MICROBUBBLE CELL ACTUATOR

by

Rebecca A. Braff

B.S. Cornell University (1996)
D.I.C. Imperial College London (1997)

Submitted to the Department of Mechanical Engineering
in partial fulfillment of the requirements for the degree of

MASTER OF SCIENCE IN MECHANICAL ENGINEERING

at the

MASSACHUSETTS INSTITUTE OF TECHNOLOGY

June 1999

Author.....
Department of Mechanical Engineering
April 16, 1999

Certified by..... 4/16/99
Martin A. Schmidt
Professor of Electrical Engineering
Thesis Supervisor

Certified by.....
Mehmet Toner
Associate Professor, Massachusetts General Hospital and Harvard Medical School
Thesis Supervisor

Certified by.....
Martha Gray
J.W. Kieckhefer Professor of Electrical Engineering
Thesis Supervisor

Accepted by.....
Ain Sonin
Chairman, Committee on Graduate Students and Reader

MICROBUBBLE CELL ACTUATOR

by

Rebecca A. Braff

Submitted to the Department of Mechanical Engineering
on April 16, 1999, in partial fulfillment of the
requirements for the degree of
Master of Science in Mechanical Engineering

ABSTRACT

The field of microsystems technology is rapidly growing, and expanding its horizons to applications in bioengineering. Currently, there are no cell analysis systems that facilitate the collection of dynamic responses for a large number of cells, and sorting based on those results. A cell chip has been fabricated in pursuit of this goal, which can capture particles in an array, hold them against a flow, and selectively release them. The release mechanism uses a vapor microbubble as a means of volume expansion to create a jet of fluid that ejects a particle. The theory, design, and testing are described, and successful operation of the device is demonstrated. Applications and suggestions for future work are discussed.

Thesis Supervisor: Martin A. Schmidt
Title: Professor of Electrical Engineering

Thesis Supervisor: Mehmet Toner
Title: Associate Professor, Massachusetts General Hospital and Harvard Medical School

Thesis Supervisor: Martha Gray
Title: J.W. Kieckhefer Professor of Electrical Engineering

Reader: Ain Sonin
Title: Professor of Mechanical Engineering

ACKNOWLEDGEMENTS

This work was sponsored by the National Science Foundation. I would like to thank my advisors, Marty Schmidt, Martha Gray, and Mehmet Toner for all of their support and guidance throughout this thesis. Working on this project has been a wonderful experience, and I thank them for giving me this exciting opportunity. Thanks to everyone in the Schmidt group for all of the help. I am particularly grateful to Joel Voldman and Samara Firebaugh for discussing all kinds of stuff with me, helping me out in the lab, and giving me really good suggestions. Thanks to Zony Chen for all of the good ideas and discussions about this work. I'd also like to thank Professor Sonin for many useful discussions and for being a reader for the thesis. I'm grateful to Professor Mikic for many discussions that helped put me on the right track. I would like to thank the Microsystems Technology Laboratories staff, particularly Kurt Broderick, for all of their aid in processing. I would like to thank Arturo Ayon and Robert Bayt for all of the advice on processing. Also, thanks to Maya Farhoud for taking some of the SEM photos.

As always, I'm indebted to my family for all of their love and support, and to Jim for helping me stay sane.

TABLE OF CONTENTS

FIGURES

TABLES

1. INTRODUCTION

As microsystems technology grows, many applications in the fields of cell biology and biomedical engineering become feasible. Scaling down to the micron level allows the use of smaller sample sizes than those used in conventional techniques. Additionally, the smaller size and ability to make large arrays of devices enables multiple processes to be run in parallel. In this thesis, a device has been designed to hold biological cells in an array, and then selectively release single cells. This device is a good example of biological micro electromechanical systems (MEMS) and could improve upon standard cell biology techniques, as well as provide new ones.

1.1 Significance

This thesis work was completed to provide a critical enabling technology for a project whose long-term goal is to create a novel cell analysis system. The system will be designed to monitor the dynamics of non-adherent cells and sort them based on those dynamics. The "μDAC" (microfabrication-based dynamic array cytometer) will combine the strengths of microscopy (time-resolved monitoring of cell behavior) and flow cytometry (high throughput), to yield an intelligent device capable of performing biological assays that are currently unavailable. As shown in Figure 1.1, the system will consist of four parts: 1) a microfabricated chip (cell-array chip) that will capture and hold many cells (~10,000) in an array; 2) a fluidic system to introduce the cells and stimuli to the chip, and to collect released cells with fraction collectors; 3) an optical system to fluorescently interrogate the cell array and record an ensemble of single-cell data; and 4) a control system to selectively release those cells that display a given behavior or signal pattern. In addition, multiple selections are possible, allowing the user to sort the initial cell population into an arbitrary number of subpopulations.[1]

The hypothesis driving this project is that the ability to monitor over time the behavior of each cell in a large population of cells will provide insight into a variety of cellular mechanisms. The system will provide this ability by combining the strengths of microscopy and flow cytometry with the enabling technology of microfabrication.

Due to the past decade's explosion in the number of optical probes available for cell analysis, the amount of information gleaned from microscopic and flow cytometric

assays has correspondingly increased. Microscopy allows the researcher to monitor (among other things) the time-response of a limited number of cells using optical probes. Flow cytometry, on the other hand, uses optical probes for assays on statistically significant quantities of cells, but can only observe each cell once, and can only easily sort a cell population into three subpopulations.

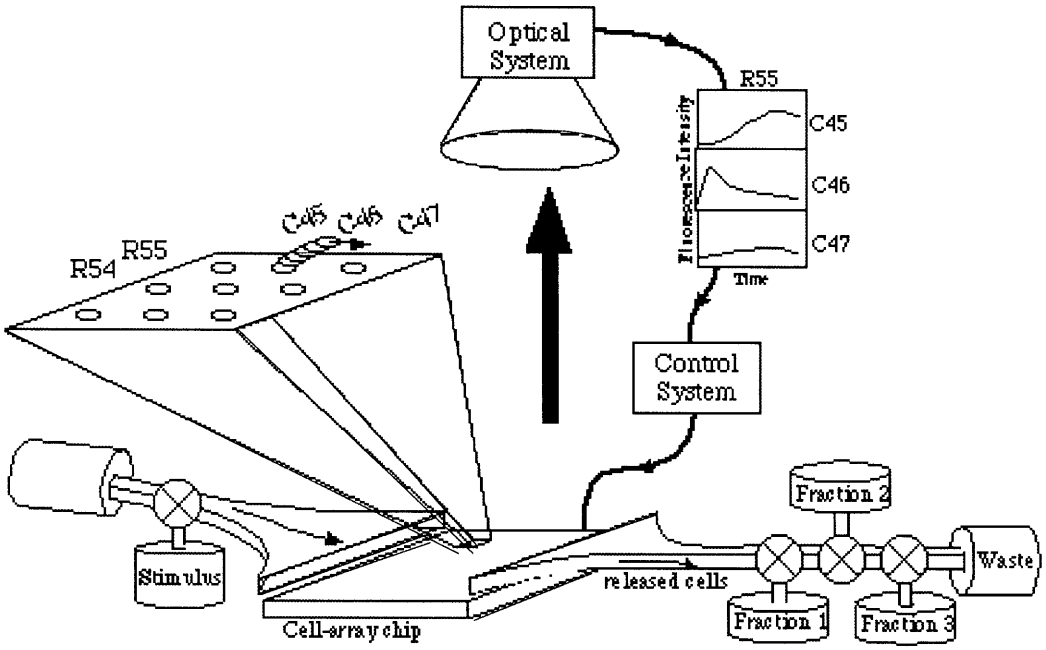

Figure 1.1 The μDAC system. (Figure by Joel Voldman)

Microfabrication is the technology that enables us to bridge these two techniques in order to fulfill our hypothesis. Using microfabrication techniques, we can build a chip that can capture, hold, and selectively release many cells in a regular array. This gives the μDAC two advantages. First, knowing the cell locations reduces the complexity of the optical and control systems dramatically, allowing us to design subsystems that can monitor the fluorescence intensity at multiple time points on many cells. Second, being able to hold and selectively release the cells lets us sort based on any aspect of their intensity-time characteristic and into arbitrary numbers of subpopulations.

Any fluorescence-based assay in which the cell's response may vary in time is a candidate for study using the μDAC. It is ideally suited for finding phenotype inhomogeneities in a nominally homogeneous cell population. Such a system could be

used by cell biologists to investigate time-based cellular responses for which assays do not currently exist. Instead of looking at the presence/absence or intensity of a cell's response to a stimulus, the researcher can look at its time response. Furthermore, the researcher can gain information about a statistically significant number of cells without having to resort to a bulk experiment. Some potential applications include the study of molecular interactions such as receptor-ligand binding or protein-protein interactions. Signal transduction pathways, such as those involving intracellular calcium, could be investigated. Geneticists could look at gene expression (such as immediate-early genes), either in response to environmental stimuli or for cell-cycle analysis. Once temporal responses to certain stimuli are determined, the system could be used in a clinical setting to diagnose disease and monitor treatment by looking for abnormal time responses in patients' cells [1].

In order to build this system, it is first necessary to create a cell-array chip that is capable of capturing, holding, and selectively releasing cells. The μDAC project is exploring two avenues of cell capture. One method is to use DEP forces (as described above) to hold cells. The second method involves the use of hydraulic forces, and is the basis of this thesis.

The applicability of the cell capture and release chip described in this thesis is wider than being used only in the μDAC. For example, it may be used to sort particles other than biological cells in applications such as toxicology screening. Additionally, experiments using the resistive heating to monitor micro-bubble formation may help us to learn more about bubble nucleation on the micro-scale, and will be discussed in more detail in later chapters.

1.2 Background

Integrated circuits have been fabricated on silicon chips since the 1950s, and as processing techniques improve, the size of transistors continues to shrink. The ability to produce large numbers of complex devices on a single chip sparked interest in fabricating mechanical structures on silicon as well. The range of applications for micro electromechanical systems (MEMS) is enormous. Accelerometers, pressure sensors, and actuators are just a few of the many MEMS devices currently produced [2-4]. Another

application of MEMS is in biology and medicine. Micromachined devices have been made for use in drug-delivery, DNA analysis, diagnostics, and detection of cell properties[5].

Manipulation of cells is another application of MEMS. The method developed in this thesis to capture, hold, and release cells using hydraulic forces draws upon previous work in cell manipulation. For example, in the early 1990's, Hitachi used pressure differentials to hold cells. [6] They microfabricated hydraulic capture chambers that were used to capture plant cells for use in cell fusion experiments. Pressure differentials were applied so that single cells were sucked down to plug an array of holes (Figure 1.2). Cells could not be individually released from the array, however, because the pressure differential was applied over the whole array, not to individual holes.

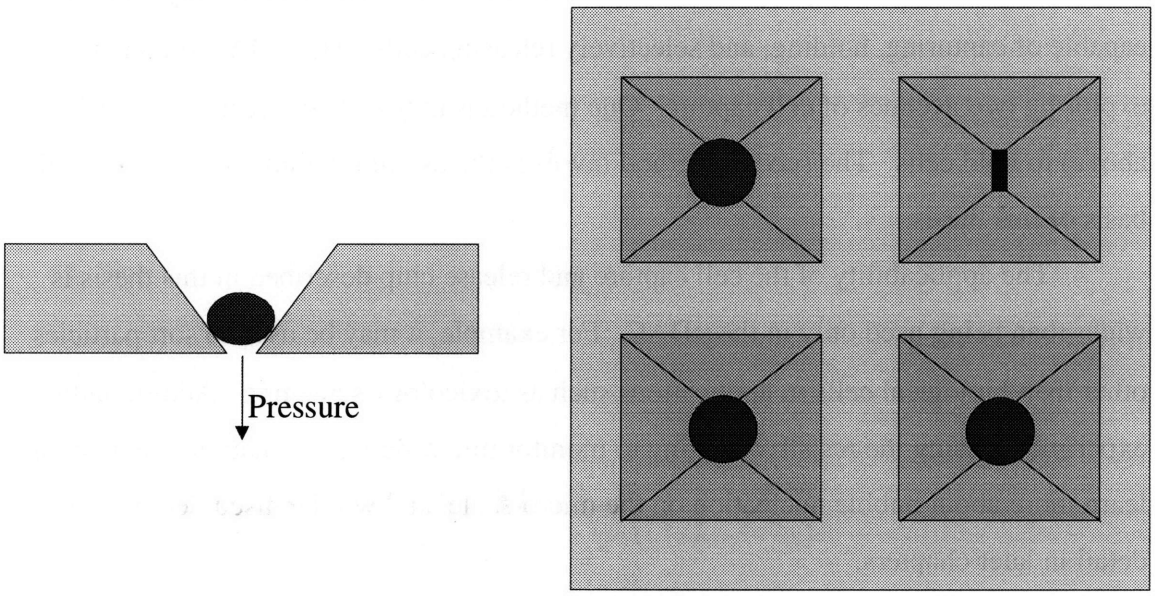

Figure 1.2 Illustration of the Hitachi cell capture plate.

Arrays of wells etched into silicon have been used by Bousse et al. [7-10] to passively capture cells by gravitational settling. Multiple cells were allowed to settle into each of an array of wells where they were held against flow due to the hydrodynamics resulting from the geometry of the wells. Changes in the pH of the medium surrounding the cells were monitored by sensors in the bottom of the wells, but the wells lacked a cell-release mechanism, and multiple cells were trapped in each well.

Another method of cell capture is the use of dielectrophoresis (DEP). DEP refers to the action of neutral particles in non-uniform electric fields. Neutral polarizable particles experience a force in non-uniform electric fields which propels them toward the electric field maxima or minima, depending on whether the particle is more or less polarizable than the medium it is in. By arranging the electrodes properly, an electric field may be produced to stably trap dielectric particles. Microfabrication has been utilized to make electrode arrays for cell manipulation since the late 1980s [11]. Researchers have successfully trapped many different cell types, including mammalian cells, yeast cells, plant cells, and polymeric particles [12-16]. However, trapping arrays of cells with the intention of releasing selected subpopulations of cells has not yet been widely explored [1].

These studies demonstrate that it is possible to trap individual and small numbers of cells in an array on a chip. Subsequent manipulation and selective release has not been demonstrated and would not be a straight-forward extension of existing technology. This inability to select or sort based on a biochemical measurement poses a limitation to the kinds of scientific inquiring that may be of interest. This thesis addresses that limitation.

The device in this thesis uses a vapor bubble as a means of cell actuation. The use of bubble formation to create a jet of fluid has been used for many years by the inkjet printer industry [17]. By using a thin-film heater to form a vapor bubble, thermal inkjet pens fire drops of ink out of chambers due to the volume expansion created by the bubble. Thermal inkjet nozzles are formed by silicon microfabrication [18, 19].

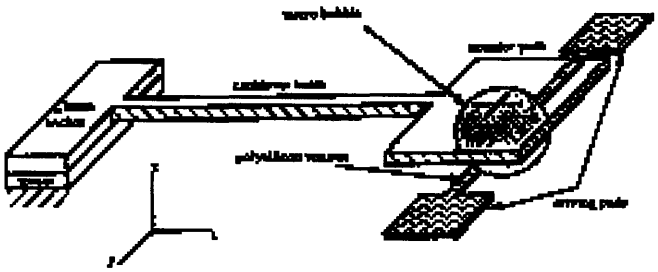

Figure 1.3 Microbubble powered actuator[20].

Vapor bubbles have also been used as a means of mechanical actuation. Lin et al.[20, 21] used microfabricated polysilicon resistive heaters to boil Fluorinert liquid and

form a vapor bubble underneath a microfabricated paddle (Figure 1.3). The vapor microbubble was found to be stable and the size was controllable within a range of currents. In this way the paddle could be moved up and down depending on the current applied to the heater. Experiments using water, however, were not equally successful because the electrolytic breakdown of water caused problems.

Evans et al. used vapor bubbles as valves and pumps in their micromixer[22]. Microbubbles were used to stop flow through a chamber, acting as valves. Bubbles were also used as a means of volume expansion to push fluid through a channel. Their use of bubbles to push fluid out of a chamber is similar to the technique used in this thesis.

1.3 Overview of Device

A schematic of the device described in this thesis is shown in Figure 1.4. A square well with a small channel in the bottom is etched in a silicon wafer. This channel connects the well to a much larger chamber on the other side of the chip. The silicon chip is attached to a glass slide on which there is a platinum heater, and the alignment is such that the heater is sealed inside the large chamber, which is filled with water.

The operation of the device is as follows. Fluid containing cells is flown over the top of the device, and then the flow is stopped. The cells then settle due to gravity and some of the cells settle into the wells (a). At this point the flow is started again, and the cells in wells are trapped, cells not in wells are flushed away by convection. (b). Experiments may now be performed on the trapped cells, e.g. by adding a reagent. When the experiments are concluded, the cells exhibiting the desired characteristics may be selectively released from the wells. This is done by applying a voltage to the resistive heaters under the silicon chip. As current flows through the resistor, it heats up due to ohmic heating (c). When the necessary temperature is reached, a vapor bubble forms and displaces a volume of fluid out of the channel in the top of the chamber (d). This jet pushes the trapped cell out into the bulk fluid, where it is entrained in the flow and flows away from the device.

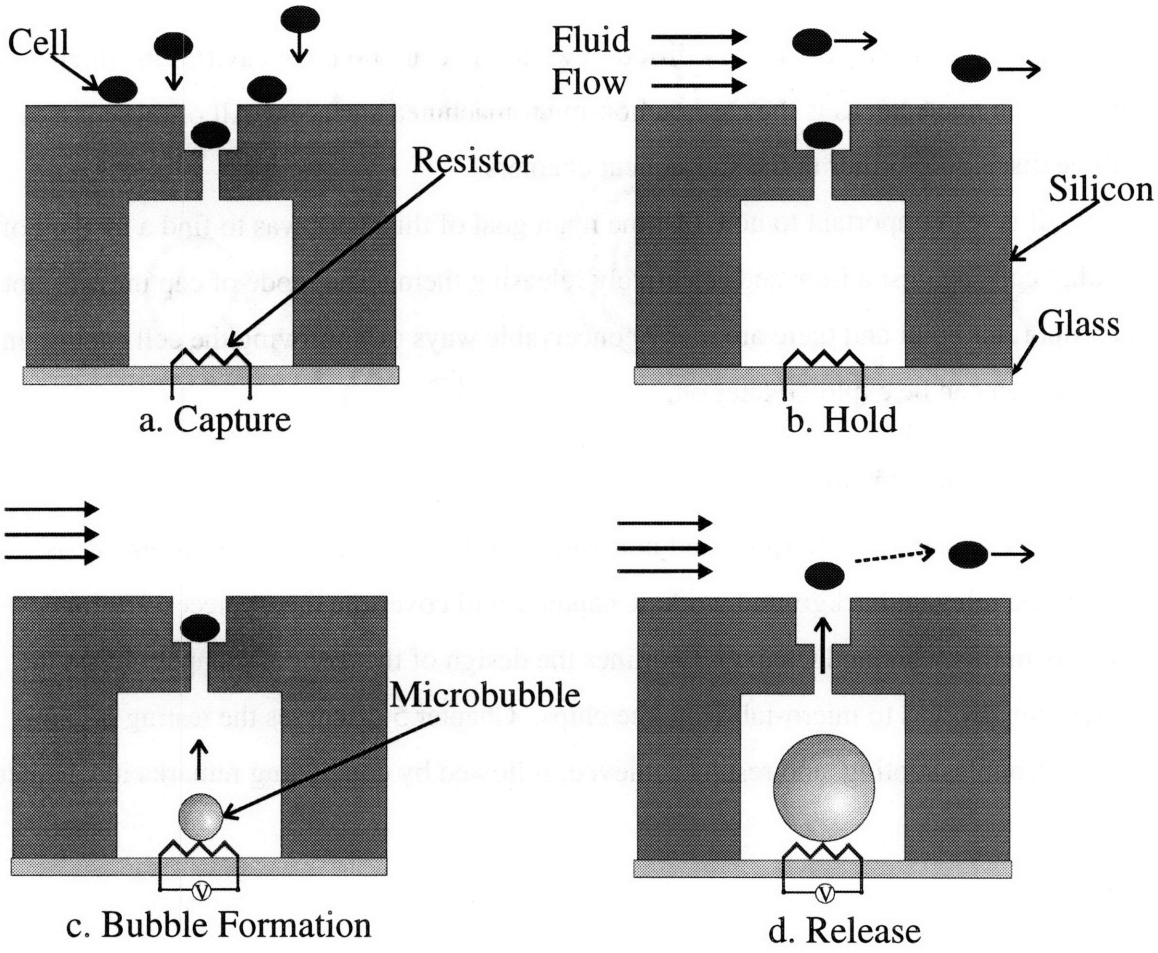

Figure 1.4 Operation of the microbubble cell actuator.

1.4 Objectives

The overall goal of this thesis is to design, build, and test a chip that can capture, hold, and selectively release particles, as described above. In order to do this, however, there are numerous intermediate steps, and many physical phenomena that must be modeled and understood.

It was necessary to design the device with the proper dimensions so that single particles could be held in wells against a flow. Biological cells were not used in these experiments, as polystyrene microspheres of the same dimensions were thought to be more robust for the initial testing. The fabrication process had to be designed in order to build chips with the desired attributes, and various problems which arose needed to be solved. It was necessary to understand the heating of the resistors so that sufficiently high temperatures could be reached. Bubble nucleation on micro-heaters was also a

challenge since the process is very different when there are no large cavities in which bubbles can nucleate, as is the case on non-micromachined surfaces. All of these issues will be discussed further in the subsequent chapters.

It is also important to note that the main goal of this work was to find a method of holding cells against a flow and selectively releasing them. The mode of capture was not the important point and there are many conceivable ways of improving the cell capture in wells which can be explored later on.

1.5 Thesis Organization

In Chapter 1, the purpose and motivation of this thesis have been discussed, as well as the relevant background work. Chapter 2 will cover the theory necessary for analysis in this work and Chapter 3 outlines the design of the device. Chapter 4 lists the fabrication process to micro-fabricate the chips. Chapter 5 discusses the testing of the device, troubleshooting, and results achieved, followed by concluding remarks in Chapter 6.

2 THEORY

This chapter will discuss the theory behind the microbubble cell actuator. First, the two regimes of bubble nucleation will be addressed, followed by a simplified heat transfer model. The fluid flow over wells and some hydrodynamic issues for the cells will be addressed as well.

2.1 Bubble Nucleation

Pool boiling takes place when a heater surface is submerged in a pool of liquid. As the heater surface temperature increases and exceeds the saturation temperature of the liquid by an adequate amount, vapor bubbles nucleate on the heater. The layer of fluid directly next to the heater is superheated, and bubbles grow rapidly in this region until they become sufficiently large and depart upwards by a buoyancy force. While rising the bubbles either collapse or continue growing depending on the temperature of the bulk fluid [23].

There are two modes of bubble nucleation: homogeneous and heterogeneous. Homogeneous nucleation occurs in a pure liquid, whereas heterogeneous nucleation occurs on a heated surface.

2.1.1 Homogeneous Nucleation

In a pure liquid containing no foreign objects, bubbles are nucleated by high-energy molecular groups. According to kinetic theory, pure liquids have local fluctuations in density, or vapor clusters. These are groups of highly energized molecules which have energies significantly higher than the average energy of molecules in the liquid. These molecules are called activated molecules and their excess energy is called the energy of activation. The nucleation process occurs by a stepwise collision process that is reversible, whereby molecules may increase or decrease their energy. When a cluster of activated molecules reaches a critical size, then bubble nucleation can occur [24].

In order to determine at what temperature water will begin to boil in the homogeneous nucleation regime, it is useful to know the thermodynamic superheat limit of water. Figure 2.1 shows the thermodynamic pressure-volume diagram.

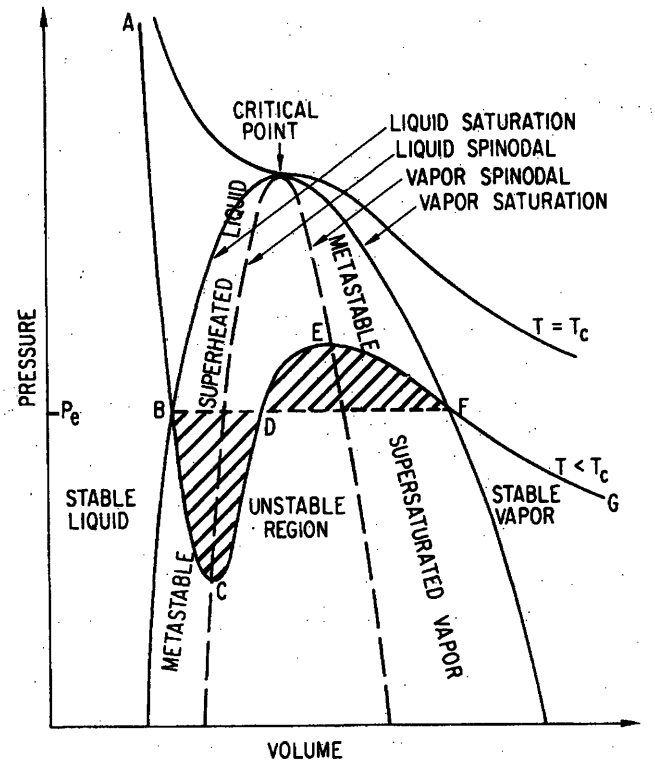

Figure 2.1 Thermodynamic pressure-volume diagram[24].

In this diagram, we can see a region of stable liquid to the far left, stable vapor to the far right, metastable regions, and an unstable region in the center of the dashed curve. The dashed line is called the spinodal, and to the left of the critical point represents the upper limit to the existence of a superheated liquid. Along this line, Equation (2-1) holds true, and within the spinodal, Equation (2-2) applies.

$$\left(\frac{\partial P}{\partial v}\right)_T = 0 \qquad (2\text{-}1)$$

$$\left(\frac{\partial P}{\partial v}\right)_T > 0 \qquad (2\text{-}2)$$

The van der Waals and Berthelot equations of state may be used to calculate the superheat limit of water, following the analysis in van Stralen and Cole [24].

$$\left(P+\frac{a}{T^n v^2}\right)(v-b)=RT \qquad (2\text{-}3)$$

Where v is the specific volume, R is the gas constant, and a and b are constants. n=0 for the van der Waals equation, n=1 for the Berthelot equation, and n=0.5 for the modified Berthelot equation. a and b may be computed using Equation (2-3), given the fact that at the critical point, Equations (2-4) and (2-5) are true.

$$\left(\frac{\partial P}{\partial v}\right)_{T_{cr}} = 0 \qquad (2\text{-}4)$$

$$\left(\frac{\partial^2 P}{\partial v^2}\right)_{T_{cr}} = 0 \qquad (2\text{-}5)$$

Using the above equations, the thermodynamic superheat limit of water may be computed. The results are shown in Table 2.1.

Equation of State	T/T_{cr} (T_{cr}=647°K)	Superheat Limit (°C)
Van der Waals	0.844	273
Modified Berthelot	0.893	305
Berthelot	0.919	322

Table 2.1 Thermodynamic superheat limit of water calculated with 3 equations of state.

These values represent the temperature above which homogeneous nucleation must begin.

A kinetic limit of superheat may also be computed using the kinetic theory of the activated molecular clusters. The kinetic limit of superheat for water is about 300°C [24].

2.1.2 Heterogeneous Nucleation

When liquid is heated in the presence of a solid surface, heterogeneous nucleation usually occurs. In this regime, bubbles typically nucleate in cavities (surface defects) on

the heated surface. The degree of superheat necessary to nucleate a bubble in a cavity is inversely dependent on the cavity radius, as shown in Equation (2-6).

$$T_w - T_{sat} = \frac{2\sigma T_{sat}}{h_{lv}\rho_v r_c} \qquad (2\text{-}6)$$

Where T_w is the surface temperature, T_{sat} is the saturation temperature (100°C for water), σ is the surface tension, h_{fg} is the latent heat of vaporization, ρ_v is the vapor density, and r_c is the cavity radius. For example, the surface temperature necessary to nucleate bubbles in water with a surface that has a 1μm cavity radius is about 133°C. For a 0.1μm cavity radius the temperature to nucleate a bubble is about 432°C, well above the highest thermodynamic water superheat limit of 322°C.

Accordingly, for surfaces with cavity sizes well below 1μm, it is likely that homogeneous nucleation will occur since the liquid will reach the superheat limit before a bubble nucleates in a cavity. Micromachined surfaces tend to have very smooth surfaces. For instance, the platinum resistors are only 3-6μm wide, and 0.1μm thick, so it is unlikely that cavities will exist on the surface which are large enough for heterogeneous nucleation to occur. The largest likely nucleation cavity would be the thickness of the resistor, which is 0.1μm, and results in a boiling temperature for heterogeneous nucleation above the thermodynamic superheat limit as shown above. Thus, we may predict that homogeneous nucleation is the method of bubble nucleation most likely to occur for the resistors in this thesis.

However, when platinum films are annealed, thermal grooving and agglomeration can take place at the grain boundaries. A groove will develop on the surface of a hot polycrystalline material where a grain boundary meets the surface. As the surface gets hotter, the grooves deepen, initiating holes, and the platinum begins the process of balling up in order to reduce surface area [25-27]. This process is called agglomeration. The agglomeration rate is insignificant at anneal temperatures below 700°C. However, for a 600°C anneal of platinum for 1 hour, the onset of agglomeration can cause small voids in

the platinum with radii of up to about 0.5μm. In this case, heterogeneous nucleation would be possible at a temperature of about 166°C.

2.2 Heat Transfer Model

It is desirable to be able to predict the electrical current necessary to achieve a certain temperature of the resistor. The system could be modeled using three-dimensional finite element analysis, but this would be computationally intensive, and analytical estimates may be made more simply. The schematic and boundary conditions for this model are shown in Figure 2.2. The dimensions and layout of the resistors will be discussed further in Chapter 3.

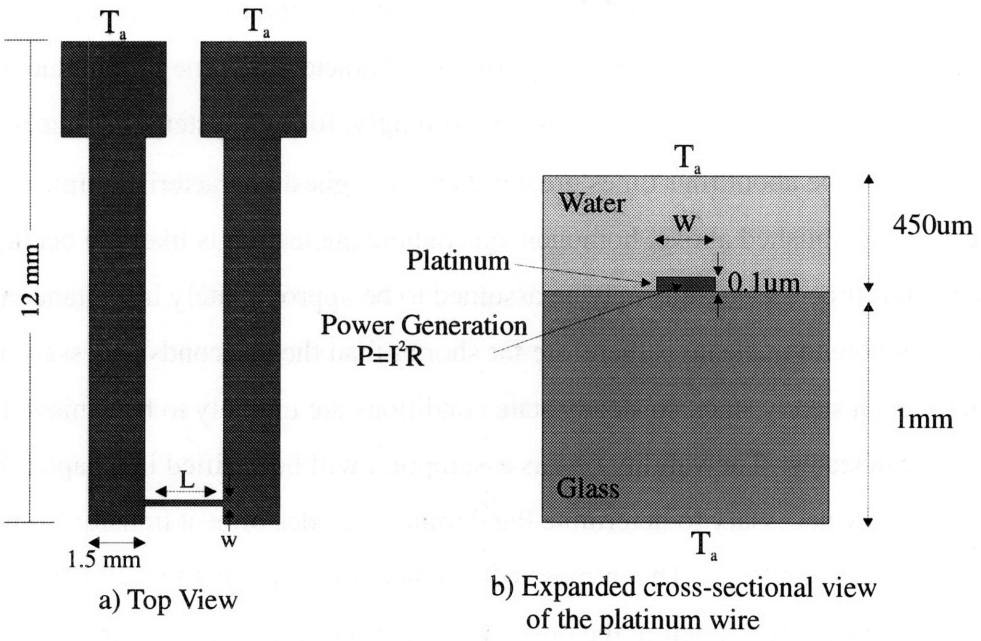

Figure 2.2 Schematic and boundary conditions for thermal model of resistor.

For the cross-sectional slice through the resistor (right), the water above the heater is 450μm thick, corresponding to the height of the silicon chamber containing the water. It is assumed that the ambient temperature is maintained at the top of the water in the well since above this there is silicon with water at the ambient temperature flowing over the top of it. The bottom of the glass slide is also assumed to be at the ambient temperature since it is contacting a surface at the ambient temperature. The resistor is about 10,000

times thinner than the glass slide and has ohmic heating, or power generation equal to I^2R for the entire volume of the resistor.

First, we may calculate the characteristic time for the heat to conduct through the two bounding surfaces using Equation (2-7).

$$\tau \approx \frac{L^2}{\alpha} \qquad (2\text{-}7)$$

Where L is the characteristic length for conduction and α is the thermal diffusivity of the material.

Using this relation, we find that the characteristic time for conduction through 1mm of glass is about 2.3 seconds. Similarly, the characteristic time for conduction through 450μm of water is 1.38 seconds. Accordingly, for this system the time to reach steady state will be about four times greater than the highest characteristic time, about 9 seconds. As established above, homogeneous bubble nucleation is likely to occur, which is a molecular process and thus may be assumed to be approximately instantaneous. The time for a bubble to nucleate is therefore far shorter than the 9 seconds necessary for the system to reach steady state, so steady state conditions are unlikely to be achieved before the bubble nucleates. The validity of this assumption will be verified in Chapter 5.

It is now necessary to determine the dominant modes of heat transfer from the resistor to its surroundings. The purpose of this model is to predict the temperature of the heater for a given current, before the onset of boiling. For this model, heat transfer due to radiation may be neglected [28]. Boiling heat transfer will not be addressed by this model.

A lumped model approach is taken for this analysis. This approximation may be checked by computing the Biot number for the resistor.

$$Bi = \frac{ht}{k_{Pt}} = 7x10^{-9} << 1 \qquad (2\text{-}8)$$

Where t is the platinum resistor thickness (0.1μm) and k_{Pt} is the thermal conductivity of platinum (71.5 W/mK). We will assume a heat transfer coefficient of $h=5W/m^2K$ as a high bound for natural convection. The Biot number measures the ratio of internal conduction resistance to external convection resistance. Since the Biot number is much less than unity, we may use the lumped body approximation and assume that the entire resistor is at a uniform temperature.

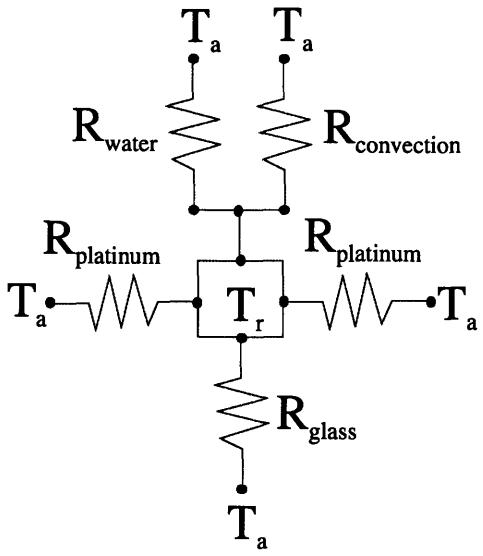

Figure 2.3 Thermal resistances seen by heater.

Figure 2.3 shows the thermal resistances between the resistor and the ambient temperature. For the purpose of this order of magnitude estimate of the heat transfer mechanisms, steady state conditions will be used in determining thermal resistances. First, the thermal resistance due to convection through the water will be computed. For this case we may assume natural convection since the water above the heater is stagnant, and boiling is not occurring. The thermal resistance due to convection is calculated below.

$$R_{convection} = \frac{1}{hA} = \frac{1}{hwL} = 6.67x10^7 \frac{K}{W} \qquad (2\text{-}9)$$

Where w is the resistor width (3μm) and L is the resistor length (1000μm).

Next the thermal resistance due to conduction through the platinum resistor, glass slide, and water may be computed. The resistance due to conduction is given by:

$$R_{conduction} = \frac{L}{kA} \qquad (2\text{-}10)$$

Where L is the length through which heat conducts, and A is the cross-sectional area. For the platinum, the length through which heat conducts is very long (12mm) and the cross-sectional area is very small, resulting in a high thermal resistance:

$$R_{platinum} = \frac{L_{Pt}}{k_{Pt} tw} = 5.4x10^{8} \frac{K}{W} \qquad (2\text{-}11)$$

Where t is the platinum film thickness (0.1μm), L_{Pt} is the length through which heat conducts (12mm), w is the width of the resistor (3μm), and k_{Pt} is the conductivity of platinum (71.5W/mK). Similarly, the thermal resistances of the glass and water are computed.

$$R_{glass} = \frac{L_g}{k_g Lw} = 4.1x10^{5} \frac{K}{W} \qquad (2\text{-}12)$$

$$R_{water} = \frac{L_w}{k_w Lw} = 2.2x10^{5} \frac{K}{W} \qquad (2\text{-}13)$$

Where L_g is the length of glass through which heat conducts (1mm), k_g is the conductivity of glass (0.81W/mK), L is the length of the resistor (1000μm), w is the width of the resistor (3μm), L_w is the length of water through which heat conducts (450μm), and k_w is the conductivity of water (0.67W/mK).

From this we can see that R_{glass} and R_{water} are the dominant thermal resistances for the system. Thus, we may neglect heat transfer due to convection in the water and conduction through the platinum.

We may now estimate the temperature of the resistor as a function of time for a given current using semi-infinite body theory. For small times (t<1ms) it may be assumed that both the water and glass are semi-infinite bodies with initial temperature T_a. At t=0, a constant heat flux (due to the resistor) is applied at the water-glass interface (x=0). The one-dimensional temperature profile may be computed using the infinite composite solid solution [29]. The region x>0 is water, x=0 is the resistor, and x<0 is the glass. A one-dimensional model may be used for short times since the length of the resistor (L=1000μm) is much less than the width of the resistor (L=6μm). The temperature can be assumed to be constant along the resistor, and lateral conduction will be neglected for small times. The validity of this model will be determined in Chapter 5, when it is compared with experimental results. The model will break down when the lateral conduction becomes significant, and when the assumption of semi-infinite bodies becomes invalid. The boundary conditions for this problem are given below.

$$T_1 = T_2, x = 0, t > 0 \tag{2-14}$$

$$\frac{q_1 \alpha_1^{\frac{1}{2}}}{K_1} = \frac{q_2 \alpha_2^{\frac{1}{2}}}{K_2}, x = 0, t > 0 \tag{2-15}$$

$$q_1 + q_2 = q \tag{2-16}$$

Where K is the thermal conductivity (0.61 W/mK for water and 0.88 W/mK for glass), q is the heat flux, and the subscript '1' denotes water, and '2' denotes glass.

The solution for the temperature profiles in water and air for a constant heat flux q (W/m^2) applied at x=0 is given by Equations (2-17) and (2-18).

$$T_1 - T_o = \frac{2q\sqrt{\alpha_1 \alpha_2 t}}{K_1\sqrt{\alpha_2} + K_2\sqrt{\alpha_1}} ierfc \frac{x}{2\sqrt{\alpha_1 t}} \tag{2-17}$$

$$T_2 - T_o = \frac{2q\sqrt{\alpha_1 \alpha_2 t}}{K_1\sqrt{\alpha_2} + K_2\sqrt{\alpha_1}} ierfc \frac{x}{2\sqrt{\alpha_2 t}} \tag{2-18}$$

Where α is the thermal diffusivity ($1.47 \times 10^{-7} m/s^2$ for water and $4.4 \times 10^{-7} m/s^2$ for glass) and T_o is the initial temperature of the body.

The solution may also be used to check the semi-infinite body assumption. For times equal to or less than 1ms, and a reasonable heat flux such as 2.5×10^7 W/m^2, the heat penetration depths into the glass and water are less than 100μm. The total thickness of the water is 450μm and of the glass is 1mm, so the semi-infinite body assumption holds true. The one-dimensional model should be sufficient for determining the temperature of the resistor at small times.

2.3 Power Calculation

Using the theory described above, we may predict the power necessary to form a bubble. Since homogeneous bubble nucleation is assumed, the bubbles will form at approximately the superheat limit of water. The value of 305°C given by the modified Berthelot equation (Table 2.1) will be used. Next, the infinite composite solid solution may be used to calculate the temperature of the heater for a given time, say 1ms. Rearranging equation (2-17) to solve for the heat flux, or power per unit area at position x=0, we get:

$$\frac{P}{Lw} = \frac{\left(K_1\sqrt{\alpha_2} + K_2\sqrt{\alpha_1}\right)(T - T_o)}{2\sqrt{\alpha_1 \alpha_2 t}} \qquad (2\text{-}19)$$

For an initial temperature of 20°C, and the other properties given above, the heat flux necessary to heat the resistor to 305°C in 1ms is computed from (2-19) to be 1.32×10^7 W/m^2. For typical resistor dimensions of w=6μm and L=1500μm, the necessary power is about 120mW.

2.4 Flow Over Wells

The micromachined wells must be of the proper dimensions to ensure that particles which settle into them remain held in the wells once a flow above them is initiated. The theory of slow viscous flow over cavities has been well characterized and the streamlines for various geometries have been calculated and experimentally verified[30-32].

Figure 2.4 shows the flow pattern for laminar flow over a rectangular cavity for two different width to height aspect ratios[32].

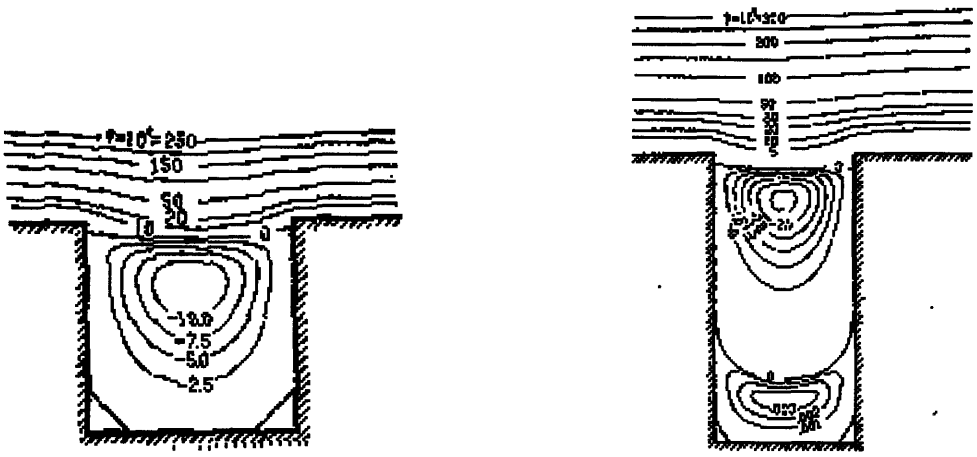

w/h=1 w/h=0.5

Figure 2.4 Flow lines for flow over rectangular cavities of given aspect ratios[32].

From these flow patterns we can see that there is a separating flow line which penetrates slightly into the cavity. Below this line there are one or two vortices, depending on the aspect ratio of the cavities. A particle below the separating flow line should not be swept out of the cavity by a slow flow in the laminar range, though the vortex may agitate the particle.

2.5 Estimate of Forces on Cells

An order of magnitude calculation was performed in order to compare the relative sizes of the gravity force pulling a particle down, compared to the viscous shear force pulling a particle out of the well. A diagram of a particle in a well with flow over the top is shown in Figure 2.5.

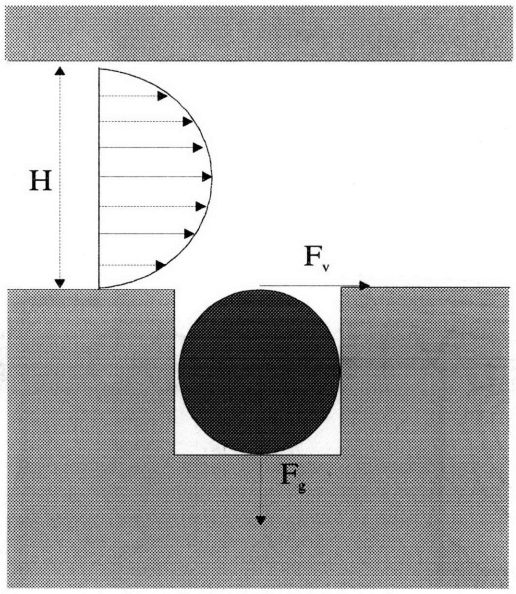

Figure 2.5 Schematic of forces on a particle in a well.

The force of gravity acting on the particle is dependent on the difference in density between the particle and the water, $\Delta\rho$. The density of water is approximately 1000kg/m^3, and the density of the polystyrene beads used in the experiments is given by the manufacturer as 1060kg/m^3. The density of cells ranges from 1050-1100kg/m^3. Accordingly, the force of gravity, F_g is computed as shown:

$$F_g = \Delta\rho \frac{4}{3}\pi a^3 g \qquad \textbf{(2-20)}$$

Where a is the particle radius (5x10^{-6}m), and g is the gravitational constant.

The viscous shear force acting on the particle is computed by assuming the top of the particle is at the top of the well, and that the flow profile is parabolic. The shear stress at the wall is:

$$\tau_w = \mu \frac{du}{dy}_{y=0} \qquad \textbf{(2-21)}$$

Where μ is the viscosity of water ($1x10^{-3}$kg/ms) and u(y) is the velocity profile as a function of y, the distance from the wall.

Assuming a parabolic velocity profile in the flow chamber, as will be discussed in Chapter 3, the flow profile may be calculated for a known chamber height and volume flow rate.

$$u(y) = \frac{6\overline{V}}{h^2} y(h-y) \tag{2-22}$$

$$\overline{V} = \frac{Q}{wh} \tag{2-23}$$

$$u(y) = \frac{6Q}{wh^3} y(h-y) \tag{2-24}$$

$$\frac{du}{dy}_{y=0} = \frac{6Q}{wh^2} \tag{2-25}$$

Where $\overline{V}$ is the average flow velocity, w is the chamber width, and h is the chamber height.

We can estimate the viscous shear force on the cell as the wall shear stress multiplied by the area being effected, approximately πa^2.

$$F_v = \tau_w \pi a^2 = \mu \frac{6Q}{wh^2} \pi a^2 \tag{2-26}$$

Where a is the cell radius. Finally the ratio of gravity to viscous force may be computed.

$$\frac{F_g}{F_v} = \frac{\Delta\rho \frac{4}{3}\pi a^3 g}{\mu \frac{6Q}{wh^2}\pi a^2} = \frac{2\Delta\rho agwh^2}{9\mu Q} \tag{2-27}$$

Using the flow chamber dimensions that will be discussed in the next chapter, and for a range of reasonable flow rates, this ratio was computed.

$$Q = 1\frac{\mu L}{\min}\left(\overline{V} = 2.1\frac{\mu m}{s}\right) \rightarrow \frac{F_g}{F_v} = 292 \quad (2\text{-}28)$$

$$Q = 10\frac{\mu L}{\min}\left(\overline{V} = 21\frac{\mu m}{s}\right) \rightarrow \frac{F_g}{F_v} = 29 \quad (2\text{-}29)$$

$$Q = 100\frac{\mu L}{\min}\left(\overline{V} = 210\frac{\mu m}{s}\right) \rightarrow \frac{F_g}{F_v} = 3 \quad (2\text{-}30)$$

It is necessary that the ratio of forces be greater than one so that the gravity force is stronger than the viscous force. These numbers may be used to aid in determining a range of acceptable operating flow rates.

2.6 Settling Time

Another relevant piece of information is the time it will take for the particles to settle. At low Reynolds number, an isolated rigid spherical particle will settle with its Stokes velocity[33].

$$U^o = \frac{2a^2(\rho_s - \rho)g}{9\mu} \quad (2\text{-}31)$$

Where a is the sphere radius (5μm for a polystyrene bead), ρ_s is the density of the bead (about 1060kg/m^3), ρ is the density of water (1000kg/m^3), and μ is the viscosity of water. Using these values we get a Stokes velocity of:

$$U^o = 5x10^{-6}\frac{m}{s} = 5\frac{\mu m}{s} \quad (2\text{-}32)$$

Using this velocity to check the associated Reynolds number we find that

$$\mathrm{Re} = \frac{\rho U^o a}{\mu} = 3x10^{-5} << 1 \quad (2\text{-}33)$$

Thus, the assumption of low Reynolds number is valid. The Reynolds number is the ratio of inertial effects to viscous forces. For this case, we are in the highly viscous regime and inertial effects are negligible.

Another value which must be checked is the Peclet number. This is the ratio of sedimentation to diffusion. For the particles to settle, the Peclet number must be sufficiently high, otherwise the particles will diffuse throughout the liquid.

$$Pe = \frac{aU^o}{D^o} \tag{2-34}$$

$$D^o = \frac{kT}{6\pi\mu a} = 4x10^{-14}\frac{m^2}{s} \tag{2-35}$$

$$Pe = 6x10^2 >> 1 \tag{2-36}$$

Where D^o is the Brownian diffusivity, and k is the Boltzmann's constant ($1.381x10^{-16}$ erg/cm). Thus the Peclet number is sufficiently high for settling to dominate over diffusion.

The value calculated above for the Stokes velocity is that for an isolated particle, however, in the case at hand there will be many beads settling at once. This is taken into account in the calculation of the hindered velocity. A function of the particle volume fraction is multiplied by the Stokes velocity to result in the hindered velocity of particles in the suspension.

$$U = U^o f(\phi) \tag{2-37}$$

$$f(\phi) = (1-\phi)^{5.1} = 0.95 \tag{2-38}$$

$$U = 4.75x10^{-6}\frac{m}{s} = 4.75\frac{\mu m}{s} \tag{2-39}$$

Where ϕ is the particle volume fraction (about 0.01 for this case). Accordingly, the time necessary for all the particles to settle to the bottom of the flow chamber may be

calculated using the hindered velocity and the chamber height, the maximum distance to be traveled.

$$t_s = \frac{h}{U} = 166s = 2.76\,\text{min} \qquad \textbf{(2-40)}$$

Where h is the chamber height (790μm). This settling time may be used as a guideline in experiments.

A more reasonable assumption for calculating the settling time is that the distance the particles fall is an average of half the chamber height. For this case we get a settling time of about 83 seconds.

2.7 Fluid Jet

For the given pressure increase associated with the bubble formation in the large sealed well, the flow rate out of the channel in the top of the well may be calculated. Since the Reynolds number is in the creeping flow regime (Re<1), inertial effects may be neglected, and the initial, instantaneous flow out of the channel may be computed using the steady state equation for flow through a circular aperture at low Reynolds number[34].

$$Q = \frac{\Delta P c^3}{3\mu} \qquad \textbf{(2-41)}$$

Where Q is the volume flow rate, ΔP is the pressure drop, c is the aperture radius (~2.5 or 4μm), and μ is the water viscosity.

Since the pressure change due to the bubble formation may not easily be calculated, we can estimate the volume flow rate out of the chamber in a different way. Because water is incompressible, we can model the bubble formation as a volume injection into the chamber resulting in the same volume being ejected from the chamber over the characteristic bubble formation time. For instance, if it takes 1ms to form a

10μm diameter bubble, then the resulting volume flow rate out of the chamber may be calculated as follows.

$$V = \frac{4}{3}\pi r^3 = 5.24x10^{-16} m^3 \tag{2-42}$$

$$Q = \frac{V}{t} = 5.24x10^{-13} \frac{m^3}{s} \tag{2-43}$$

Using the volume flow rate we may now calculate the average velocity of fluid out of the channel, and check that the Reynolds number of the flow is indeed low.

$$\overline{V} = \frac{Q}{\pi c^2} = 27 \frac{mm}{s} \tag{2-44}$$

$$\mathrm{Re} = \frac{\rho \overline{V} c}{\mu} = 0.067 < 1 \tag{2-45}$$

Where c is the channel radius (2.5μm). The force of the fluid jet on the particle may now be calculated using the Stokes drag force:

$$F_D = 6\pi\mu a\overline{V} = 2.5x10^{-9} N \tag{2-46}$$

Where a is the radius of the spherical particle (5μm for polystyrene beads). Comparing this to the gravitational force (2-20) pulling the particle down, we find that the force of the jet on the particle is much greater than the force of gravity.

$$F_g = \Delta\rho \frac{4}{3}\pi a^3 g = 3.1x10^{-13} N << F_D \tag{2-47}$$

$$\frac{F_D}{F_g} \propto \frac{\overline{V}}{a^2} \tag{2-48}$$

Where $\Delta\rho$ is the difference in densities between the water and the polystyrene beads (60 kg/m^3). We can see that as the particle radius increases, the effect of gravity increases. For typical cells, the radius ranges from 5μm (red blood cells) to 20μm (most other cells) to 100μm (embryos and eggs). This device will most likely be used for cells on the order of 5-10μm in radius so the above calculation is representative of the expected applications.

3 DESIGN

It was necessary to decide the best way to design each component of the microbubble cell actuator. What follows are the details of the design of the resistive heaters, cell-capture wells, photolithographic masks, and flow chamber.

3.1 Resistive Heaters

In order to heat the water to a sufficiently high temperature for microbubble formation, resistive heaters are used. The heaters are made of thin-film platinum on standard glass slides. Details of the fabrication of the resistors may be found in Chapter 4.

In the design of the heaters it was necessary first to determine a range of resistances and currents to attain the desired power output. The design constraint for this step was the need to keep the current density below the electromigration limit of platinum, while retaining an adequate degree of ohmic heating. The electromigration limit is the maximum current density which platinum can endure before the atoms begin to migrate leaving the resistor inoperable.

The electromigration limit of platinum was reported to be $J=9x10^6$ A/cm^2 [35]. It was necessary to design the resistors to operate at a current density below this limit.

The resistance of a line heater is calculated as follows.

$$R = \frac{\rho L}{tw} \qquad (3\text{-}1)$$

Where R is the resistance (Ω), L is the length of the resistor (m), t is the film thickness (m), w is the width of the resistor (m), and ρ is resistivity of platinum (Ωm).

The power output of a resistor is a function of the current and resistance, as shown below.

$$P = I^2 R \qquad (3\text{-}2)$$

$$J = \frac{I}{wt} < 9x10^6 \frac{A}{cm^2} \qquad (3\text{-}3)$$

Where I is the current (A) and J is the current density.

Accordingly, as the currents were limited by the electromigration limit, the resistances needed to be sufficiently high to achieve the desired power output. The power output necessary to form a bubble was estimated by using the numbers from Lin et al.'s paper, 'Microbubble Powered Actuator'[20], where microbubbles were formed on a polysilicon line heater. Their resistor was on top of a thin dielectric layer, which was on a silicon wafer. It is reasonable to assume that the heat dissipation of this configuration might well be greater than the heat dissipation of the platinum line resistor fabricated on a glass slide. Also, a liquid with a higher boiling point by 70°C (Fluorinert-43) was used. The power necessary to nucleate bubbles under these conditions was approximately 65mW [20].

Slide Name	Resistor	Length (um)	Width (um)	Resistance (Ohms)	Electromigration Limit (mA)	Max Power (mW)
Slide1	1	3000	3	1000	22	467
	2	2500	3	833	22	389
	3	500	3	167	22	78
	4	1000	3	333	22	156
	5	1000	4	250	29	207
	6	2000	3	667	22	311
	7	1500	3	500	22	233
	8	1000	5	200	36	259
Slide2	1	3000	3,6	483	22	226
	2	2500	3,6	400	22	187
	3	500	3	167	22	78
	4	1000	3,6	150	22	70
	5	1000	6	167	43	311
	6	2000	3,6	317	22	148
	7	1500	3,6	233	22	109
	8	1000	3,5	180	22	84
Slide3	1	3000	6	625	43	1166
	2	2500	6	521	43	972
	3	500	3	208	22	97
	4	1000	3	417	22	194
	5	1000	6	208	43	389
	6	2000	6	417	43	778
	7	1500	6	313	43	583
	8	1000	6	208	43	389

Table 3.1 Resistor dimensions, resistances, and electromigration limits.
(Entries such as (3,6) refer to w=3 in the 100μm narrow region and w=6 elsewhere)

Using this as a guideline, the resistances were chosen to range from 167Ω-1000Ω, yielding maximum powers before electromigration of 70-1166mW. These powers were chosen to be up to an order of magnitude greater than necessary to avoid reaching the electromigration limit in the operation of the resistors.

The resistivity of platinum actually varies with temperature and film deposition conditions, and will be discussed in Chapter 5, but for these calculations it was taken to be $1x10^{-7}\Omega m$ [36]. This is the value for bulk platinum, however the resistivity of thin film platinum can vary widely. Heater widths range from 3 -6μm and lengths range from 500 -3000μm. Some heaters were designed to have a narrow region, 100μm long in the center, which would be hotter than the rest of the resistor. The diagrams of the two heater configurations are shown in Figure 3.1. A table of resistor dimensions, maximum currents, and maximum power outputs is also shown in Table 3.1.

The lines connecting the contact pads to the heaters were designed to have a far lower resistance than the heaters. This is done to ensure that the lines do not heat up, and that they remain approximately at the ambient temperature. The connector line widths were chosen to be 1500μm with lengths of 12mm. The total resistance of each line is about 7.7Ω.

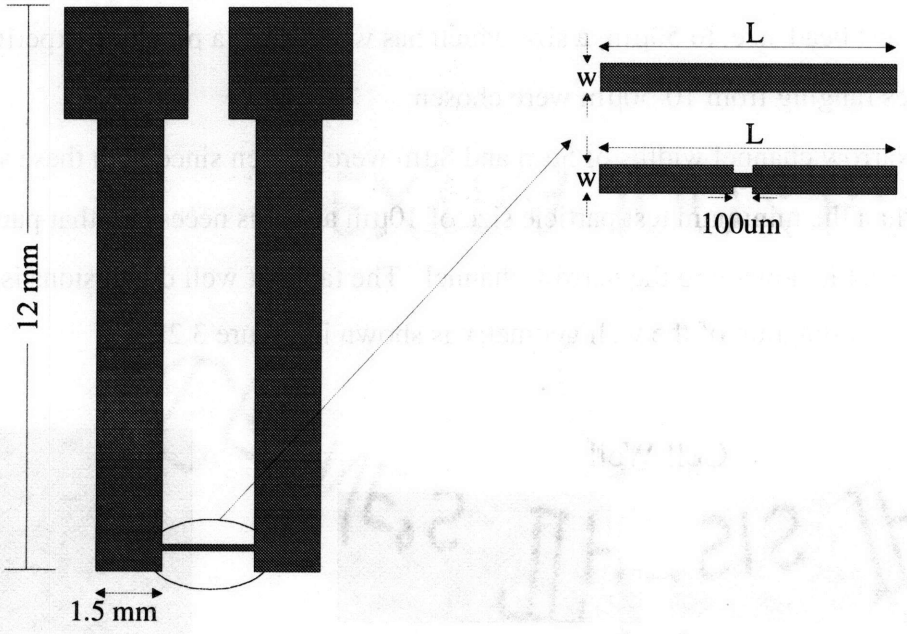

Figure 3.1 Resistor diagram and dimensions.

3.2 Cell Wells

Square wells are micromachined into silicon in order to hold cells. It was necessary to choose a range of dimensions for these wells to allow for tests with different particle sizes and flow rates. The final goal was to have the ability to trap one particle in each of an array of wells.

Chip Number	Well Dimension (um)	Hole Dimension (um)
1	16	5
b	16	8
2	10	5
2b	10	8
3	20	5
3b	20	8
4	30	5
4b	30	8
5	40	5
5b	40	8
6	50	5
6b	50	8

Table 3.2 Well dimensions

Side lengths of the wells were chosen to range from 10μm, corresponding to the smallest test bead size, to 50μm, a size which has worked for a previous experiment [7]. Well sizes ranging from 10-50μm were chosen.

Narrow channel widths of 5μm and 8μm were chosen since both these sizes are smaller than the minimum test particle size of 10μm and it is necessary that particles not be able to settle down into the narrow channel. The table of well dimensions is shown in Table 3.2. A diagram of the well geometry is shown in Figure 3.2.

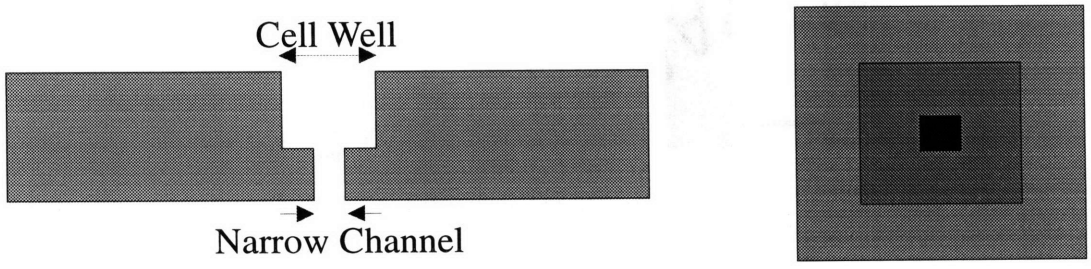

Figure 3.2 Well diagram.

3.3 Mask Design

Photomasks for use in the device fabrication were created using standard mask layout software. The mask set for the silicon processing are shown in Figure 3.3 and the glass mask set is shown in Figure 3.4.

Three masks were designed for the silicon portion of the device processing. One mask was created for the cell wells, one for the narrow channels within the wells, and one for the large wells etched from the backside of the wafer to enclose the heaters.

Two masks were made for the fabrication of the platinum heaters on the glass slides. One mask was designed to pattern the metal and the other mask was designed to pattern photoresist on top of the metal for a bonding technique. This second mask was deemed unnecessary later on, and was not used. More processing details may be found in Chapter 4.

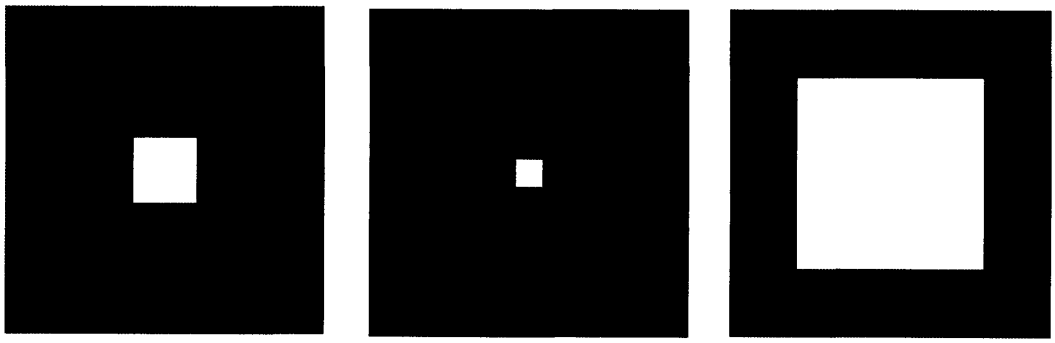

Figure 3.3 Silicon processing mask set.

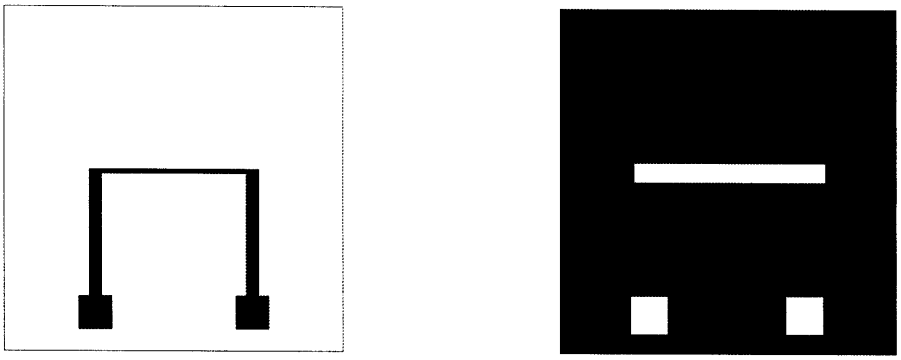

Figure 3.4 Glass processing mask set.

3.4 Flow System Design

In order to test the finished devices, a fluidic system was designed and assembled. (Figure 3.5) A syringe pump is used as the flow source for the bulk fluid, and flow rates ranging from 1 to 100 μL/min may be specified. Beads, cells, or cell stimuli may be injected through the sample injection valve. A pressure sensor is located before the flow chamber so that the pressure drop across the chamber may be monitored. Sharp increases in the pressure drop are often caused by problems in the flow chamber, such as air bubbles or other blockages. The flow chamber holds the device chip and will be further explained later. All fluid is outlet into a waste beaker which may be reused if desired.

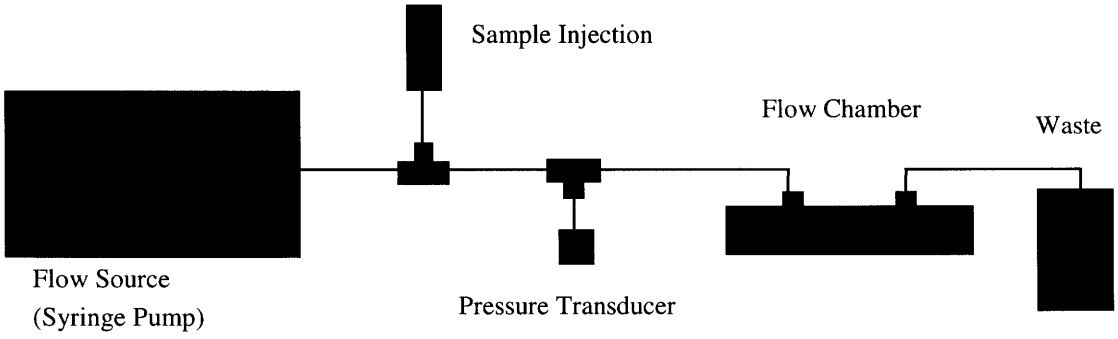

Figure 3.5 Flow system for device testing.

A schematic of the flow chamber is shown in Figure 3.6. The flow chamber is machined from plexiglass so that it is clear and a microscope may be used to observe cell behavior from above the chamber. HPLC (high-performance liquid chromatography) fittings are used with tube dimensions of 1/16 inch outer diameter and 0.020 inch inner diameter. The majority of the pressure losses are due to the tubes, not the flow chamber. The gasket between the slide and the top cover is made from PDMS (poly dimethyl siloxane), a flexible polymer. A seal is formed by screwing the top plate down onto the bottom plate. Aluminum molds were machined in order to create PDMS gaskets of the proper dimensions. Gaskets are compressed until a hard stop is reached. The stop is provided by the spacers, made of metal shim stock, in order to accurately specify the channel height. The aspect ratio of the channel's width to height is greater than 10, allowing the assumption of a parabolic velocity profile- plane Poiseuille flow.

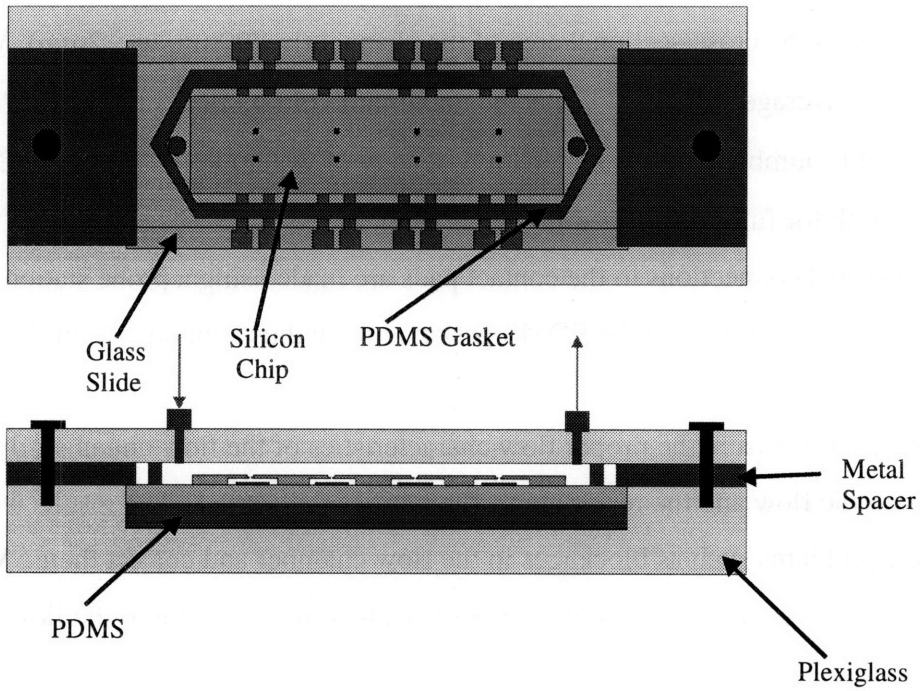

Figure 3.6 Flow chamber diagram.

The height of the flow chamber is 790μm (determined by thickness of metal spacer). Flow rates ranging from 1 to 100 μL/min correspond to Reynolds numbers of 0.001-0.1. In this creeping flow regime, the entrance length for fully developed flow was calculated to be negligible. These calculations are shown below.

$$\overline{V}_{\min} = \frac{Q_{\min}}{A_c} = 1.77 \frac{\mu m}{s} \quad (3\text{-}4)$$

$$\overline{V}_{\max} = \frac{Q_{\max}}{A_c} = 177 \frac{\mu m}{s} \quad (3\text{-}5)$$

$$\mathrm{Re}_{\min} = \frac{hV_{\min}}{\nu} = 0.0011 \quad (3\text{-}6)$$

$$\mathrm{Re}_{\max} = \frac{hV_{\max}}{\nu} = 0.11 \quad (3\text{-}7)$$

$$X_e \approx \frac{h\mathrm{Re}_{\max}}{30} = 2.6\mu m \quad (3\text{-}8)$$

Where $\overline{V}_{min}$ is the minimum average velocity, Q_{min} is the minimum volume flow rate (1μL/min), A_c is the cross-sectional area of the channel (h=790μm, w=12mm), V_{max} is the maximum average velocity, Q_{max} is the maximum volume flow rate (100μL/min), Re is the Reynolds number, ν is the kinematic viscosity of water ($1x10^{-6}m^2/s$), and X_e is the entrance length for fully-developed flow.

Electrical connections to the contact pads are made using a probe station. Contact pads are positioned outside of the PDMS gasket and are thus kept outside of the fluid flow.

In order to ensure the proper flow characteristics of the flow chamber, dye was injected into the flow and the resulting profile has been observed. The results were used to discover problems such as blockages in the flow chamber and correct them. When a uniform flow was established, 10μm diameter beads were injected into the flow and observed under a microscope.

The pressure drop across the flow chamber was monitored using a pressure transducer. The majority of the pressure drop was caused by the connector tubing, but by comparing the pressure reading to the theoretical value, the presence of bubbles and other blockages to the flow may be detected.

The pressure versus flow rate plot for the flow chamber is shown in Figure 3.7. The theoretical value is plotted with the experimental measurements. When these two values do not match, a blockage in the chamber or tubing is probable.

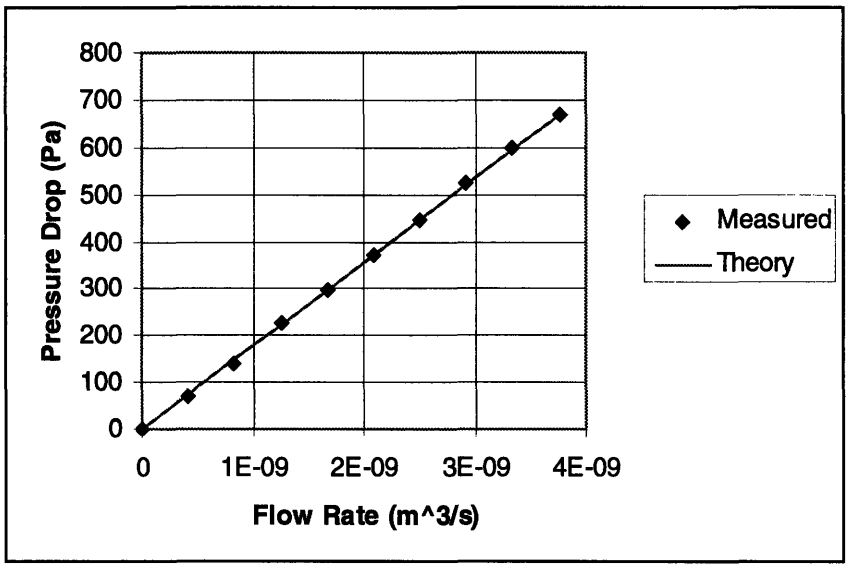

Figure 3.7 Pressure drop vs. flow rate for the flow chamber.

The pressure drop through the tubing was calculated using the following equation.

$$\Delta P = \frac{-8\mu Q}{\pi r^4}\Delta x \qquad (3\text{-}9)$$

Where μ is the viscosity of water ($1x10^{-3}$kg/ms), r is the tube radius (0.254mm), and Δx is the tube length (m). The pressure drop through the chamber was calculated to be negligible in comparison.

The flow chamber schematic with dimensions is shown in Figure 3.8.

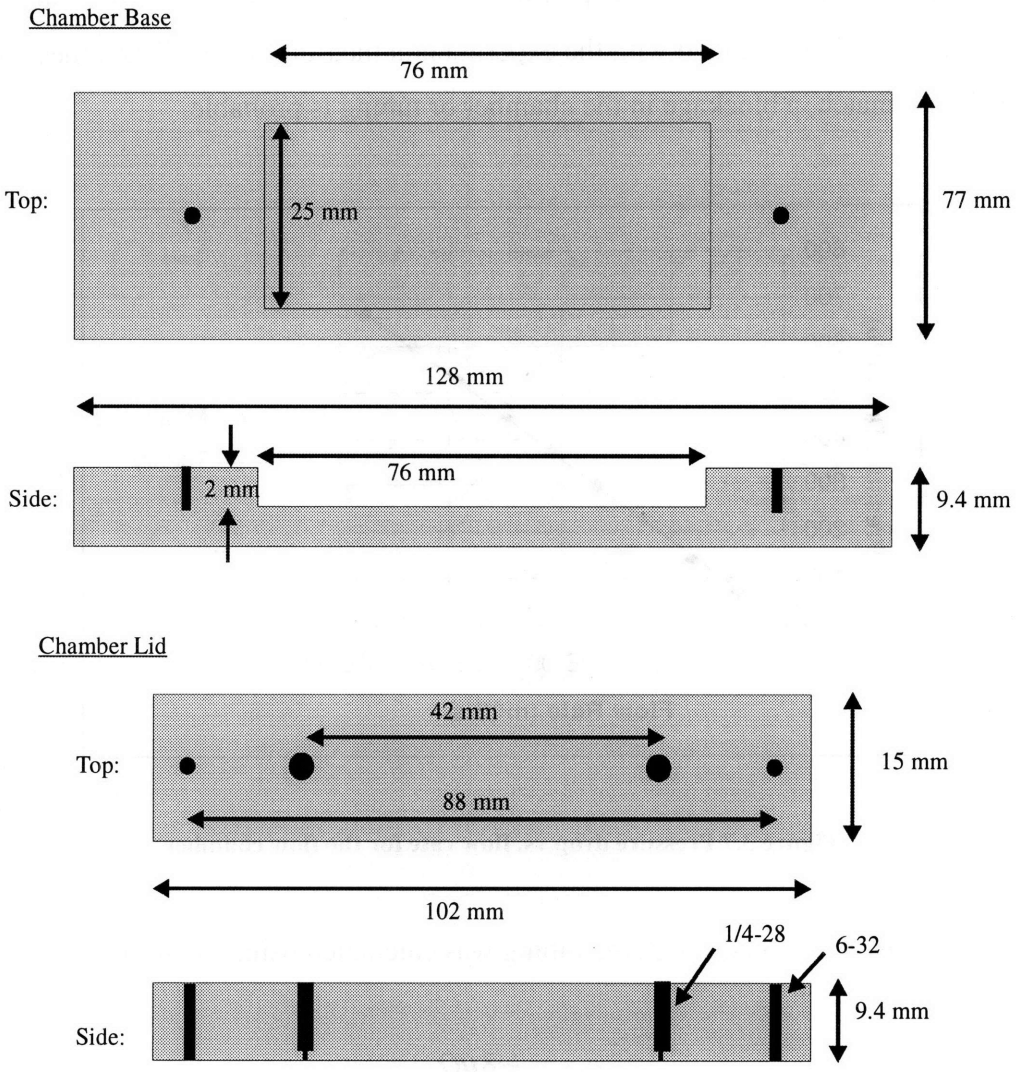

Figure 3.8 Flow chamber schematic with dimensions.

4 FABRICATION

4.1 Glass Slides

The platinum heaters are fabricated on standard 1x3in glass slides using a lift-off process. The process flow is shown below in Figure 4.1. In the first step (Figure 4.1a), photoresist is spun onto the glass slide, exposed using mask 4, and developed. Next, 100Å of titanium and 1000Å of platinum are evaporated onto the slide (Figure 4.1b). The titanium serves as an adhesion layer between the glass and the platinum. In the following step, the slide is submerged in acetone to dissolve the photoresist and lift away the metal which was deposited on top of the photoresist (Figure 4.1c). Only the platinum resistors are left on the glass slide. Some slides were then annealed in a tube furnace at 600°C for 1 hour. Finally photoresist may be deposited, exposed with mask 5 and developed to use to attach the silicon chip to the slide. This step is optional and was not used since wet photoresist may be applied manually to the slide to accomplish the same purpose. This will be discussed further at the end of the chapter. A full listing of the process steps for the glass slides may be found in Appendix A.

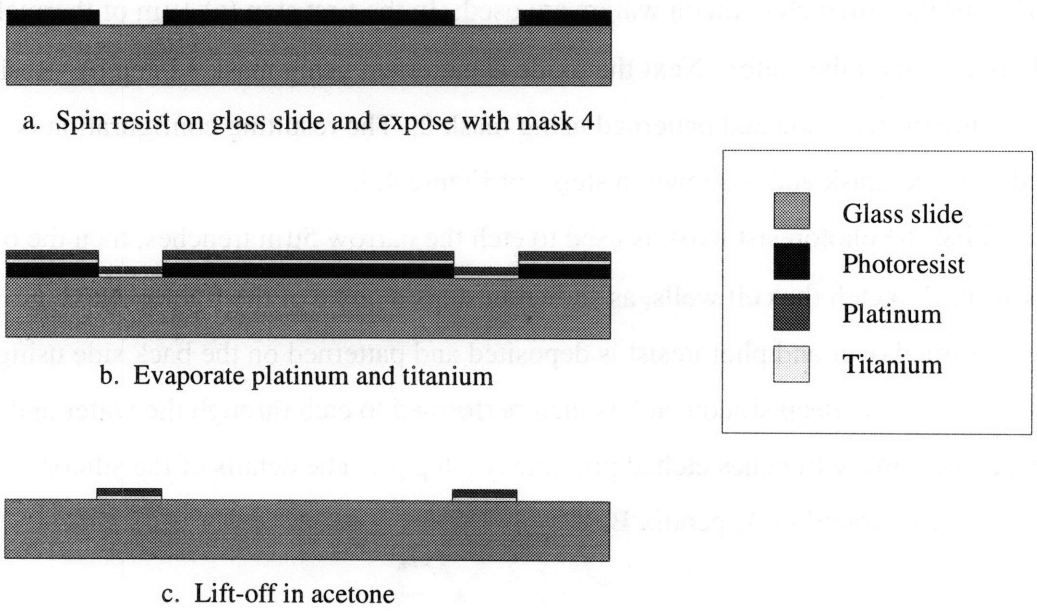

Figure 4.1 Glass slide process flow.

A photograph of a finished resistor is shown in Figure 4.2.

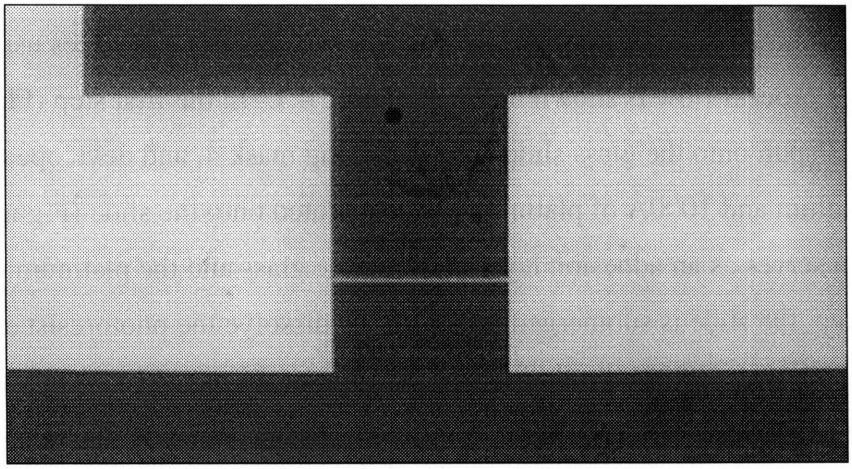

Figure 4.2 A finished resistor.

4.2 Silicon Chips

The silicon chip process flow is shown in Figure 4.3. Double Side Polished (DSP) four inch diameter silicon wafers are used. In the first step (a) 1μm of thermal oxide is grown on the wafer. Next the oxide is patterned using mask 1 (step b). Resist is spun on top of the oxide and patterned using mask 2. The resulting configuration is called a nested mask and is shown in step c of Figure 4.3.

First the photoresist mask is used to etch the narrow 5μm trenches, then the oxide mask is used to etch the cell wells, as shown in steps d and e of the figure. Next the wafer is turned over and photoresist is deposited and patterned on the back side using mask 3 (step f). A deep silicon etch is then performed to etch through the wafer and intersect the narrow trenches etched previously (step g). The details of the silicon process may be found in Appendix B.

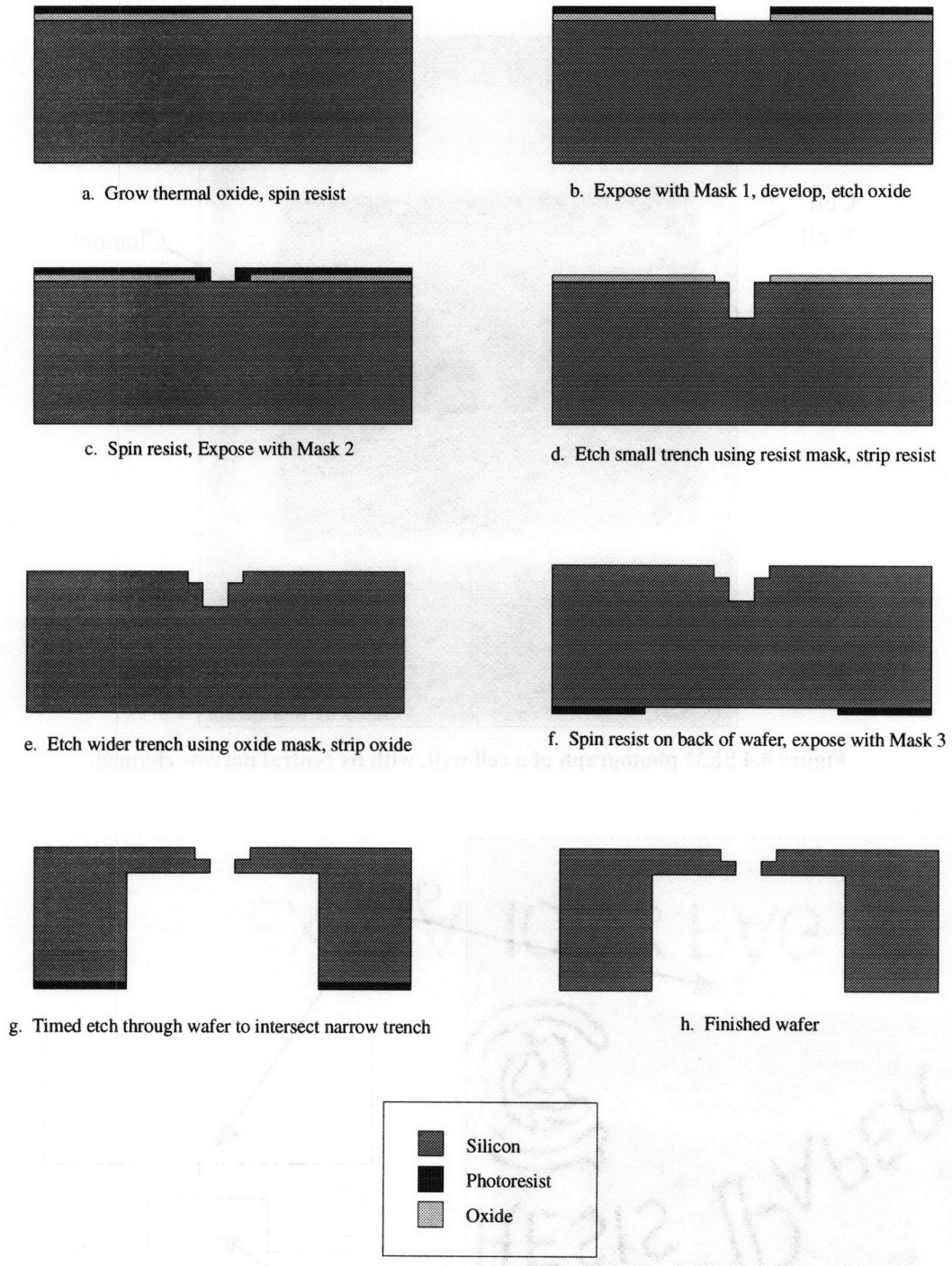

Figure 4.3 Silicon process flow.

Pictures taken in an SEM (scanning electron microscope) of the silicon wells are shown in Figure 4.4 and Figure 4.5.

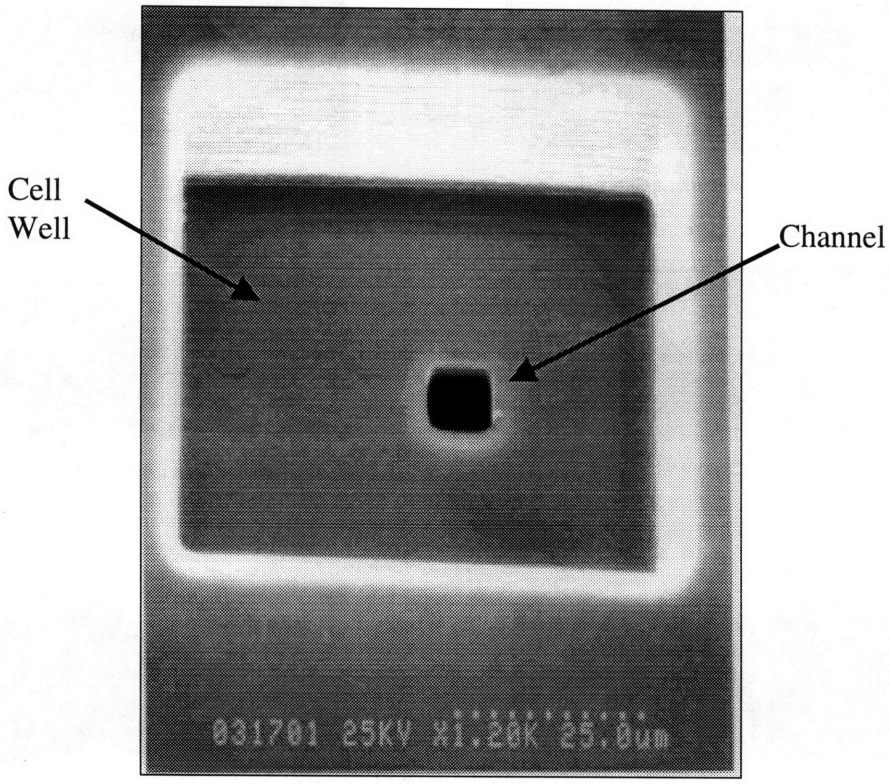

Figure 4.4 SEM photograph of a cell well, with its central narrow channel.

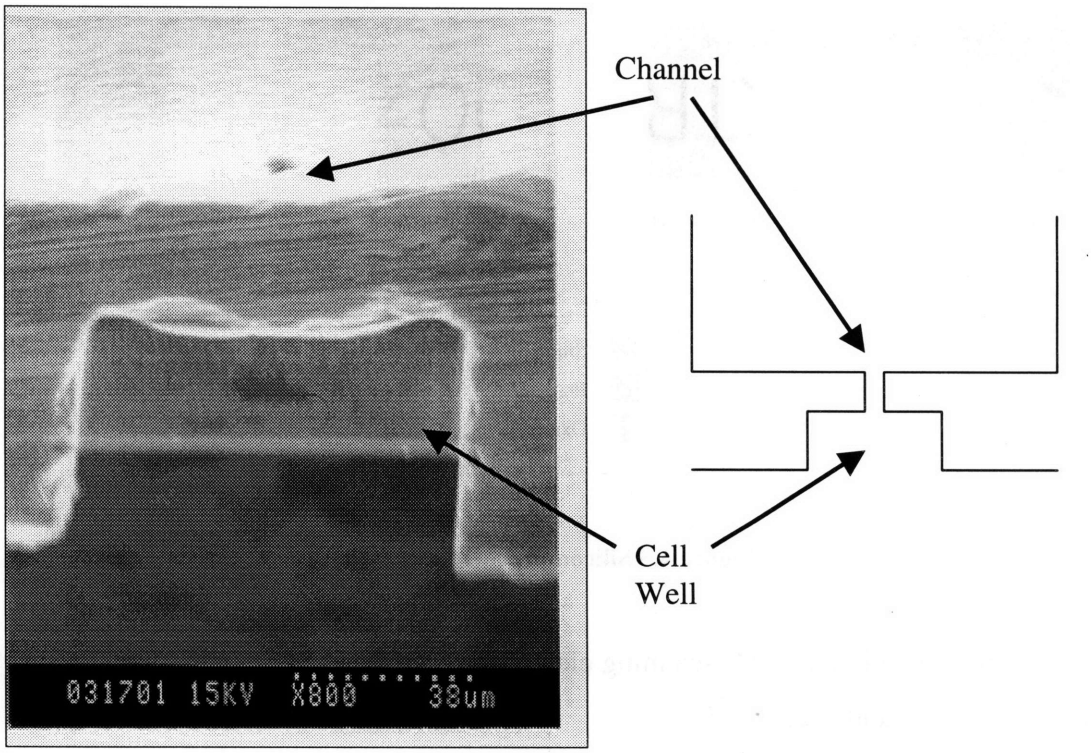

Figure 4.5 SEM photograph of cell well cross-section, with narrow channel.

4.3 Device Assembly

A complete device consists of a silicon chip attached to a glass slide by photoresist (Figure 4.6). The resist provides a water-tight seal so that volume expansion in the bubble wells results in a burst of fluid being pushed through the narrow channel and ejecting a cell.

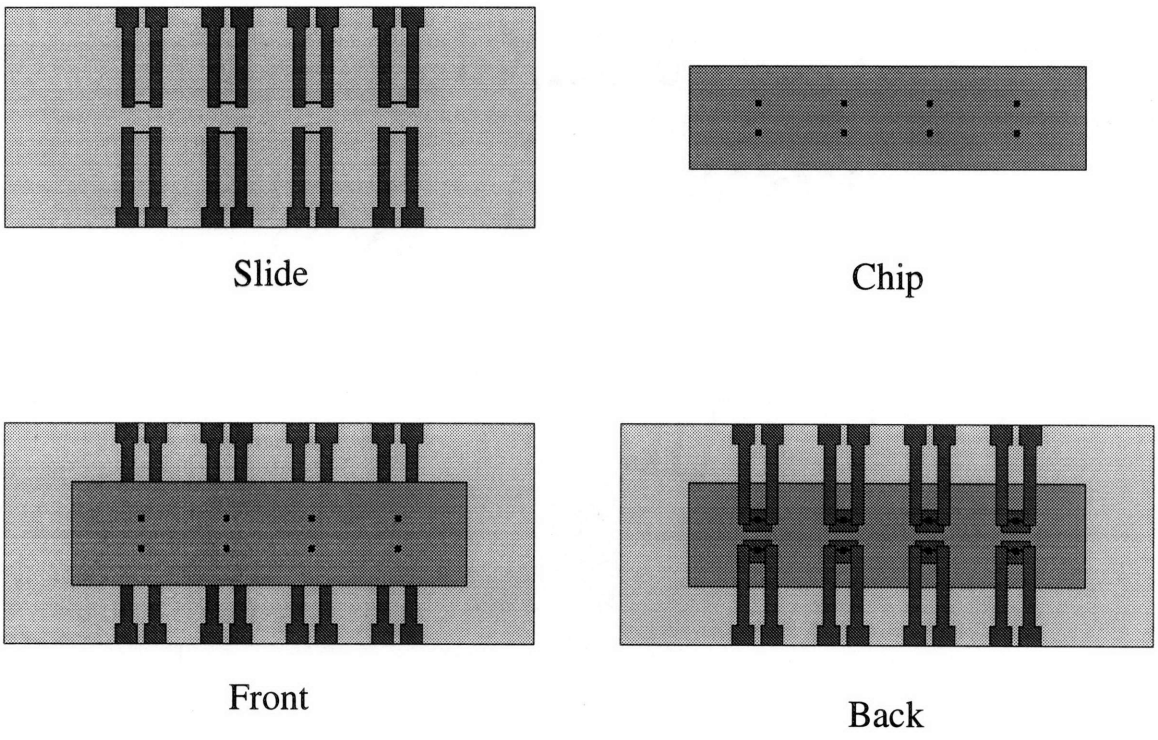

Figure 4.6 Fully assembled device.

To facilitate the assembly process, alignment marks were fabricated on the glass slide and matching holes were etched in the silicon chip. The alignment tolerances are sufficiently large (about 2mm) that the chip may be aligned to the slide by hand using just the naked eye, while still positioning the bubble wells over the platinum heaters.

Initially it was planned to deposit and pattern photoresist on the glass slide and then stick a silicon chip wet with acetone down onto the slide to attach them. This was unnecessarily complicated, however, and a simpler method was devised. Photoresist is painted onto the silicon chip around the bubble wells using a toothpick. Drops of water are deposited into each well using a pipette, then the glass slide is visually aligned from

above and stuck down onto the chip. The drops of water serve to fill the bubble wells and get pushed through the narrow channel to fill it with water. The device is now ready to be tested in the flow chamber.

5 RESULTS

5.1 Resistor Characterization

Although the resistances of the heaters were calculated in Chapter 3, it is to be expected that the measured values vary somewhat. Reasons for variation are as follows. The photolithography, i.e. the patterning of the glass slides and development can result in line widths different by several microns from the mask dimensions. Over-developing results in wider lines, and exposure times can also change results. Increasing the uncertainty is that the optical measurement of line width can vary by about a micron due to the limitations of the human eye looking through a microscope, and the fact that the measurements are diffraction-limited. The thickness of the thin film platinum is also variable, however, this thickness can be measured with reasonable accuracy using a profilometer. As was mentioned in Chapter 3, the resistivity of thin film platinum is also a variable quantity. Accordingly, deviations from the predicted resistance can be caused by multiple unknowns.

The film thickness was first measured using a profilometer. The platinum thickness measurements ranged from about 800-900Å, so the average value of 850Å will be used in the subsequent calculations.

Next, the resistance along metal lines wide enough not to be strongly affected by variation of a few microns was measured using a multimeter. The lines used for this measurement were measured in an optical microscope to be about 1510μm wide. The length of the lines was about 8mm. Knowing the width, thickness, and length of these lines, as well as the measured resistance, we can solve for the resistivity of the thin film platinum at room temperature. The measured resistance was 15Ω, and the computed resistivity is shown below.

$$\rho = \frac{twR}{L} = 2.41x10^{-7}\,\Omega m \qquad (5\text{-}1)$$

Where t is the film thickness (850Å), w is the line width (1513μm), R is the measured resistance (15Ω), and L is the length of the line (8mm). This resistivity is more than

twice the value for bulk platinum ($1x10^{-7}$ Ωm), but is a reasonable value for thin film platinum. This is because bulk platinum is a crystalline material, whereas thin film platinum is polycrystalline and the grain boundaries significantly increase resistance.

Next, the resistance of the resistors was measured with a multimeter. Using the value of resistivity from above, we can solve for the line width of each resistor. The line widths were also measured using an optical microscope to an accuracy of about ±1μm, thus if the line widths resulting from the use of the resistivity are very different than the optical measurements, the resistivity is probably wrong. The results of this measurement for two different resistor slides are shown in Table 5.1.

	Resistor #	L (um)	R (Ohms)	Computed Line Width (um)	Measured (um)	Design (um)
Slide 1	1	3000	1020	8.34	8	3
	2	2500	845	8.39	8	3
	3	500	185	7.66	8	3
	4	1000	347	8.17	8	3
	5	1000	272	10.42	10	4
	6	2000	672	8.44	9	3
	7	1500	504	8.44	8	3
	8	1000	260	10.90	10	5
Slide 3	1	3000	850	10.01	10	6
	2	2500	728	9.74	10	6
	3	500	247	5.74	6	3
	4	1000	479	5.92	6	3
	5	1000	316	8.97	9	6
	6	2000	620	9.15	9	6
	7	1500	450	9.45	10	6
	8	1000	270	10.50	10	6

Table 5.1 Resistance measurements and calculated, measured, and designed line widths.

From this we can see that the measured and calculated line widths are within the range of error for the measurements, confirming the resistivity calculation. Also, the line widths are much larger than the designed values on the masks. This is a result of over-developing in the photolithography stage of processing. (see Chapter 4)

The variation in resistivity of the platinum with temperature was mentioned previously and must now be addressed. Resistor #5 on Slide 3 was used for resistance measurements at varying temperature. The glass slide was placed on a metal block on top of a hotplate. Alligator clips were used to connect the multimeter probes to the ends of the metal line for the resistance measurements. A thermocouple was soldered to the

top surface of the glass slide near the resistor to monitor the temperature. Resistance measurements were taken for a range of temperatures.

The resulting plot of normalized resistance versus temperature is shown in Figure 5.1. The resistance is normalized using the resistance at room temperature. This curve can be used later to predict the temperature of a resistor, knowing the resistance at room temperature and measuring the resistance during operation.

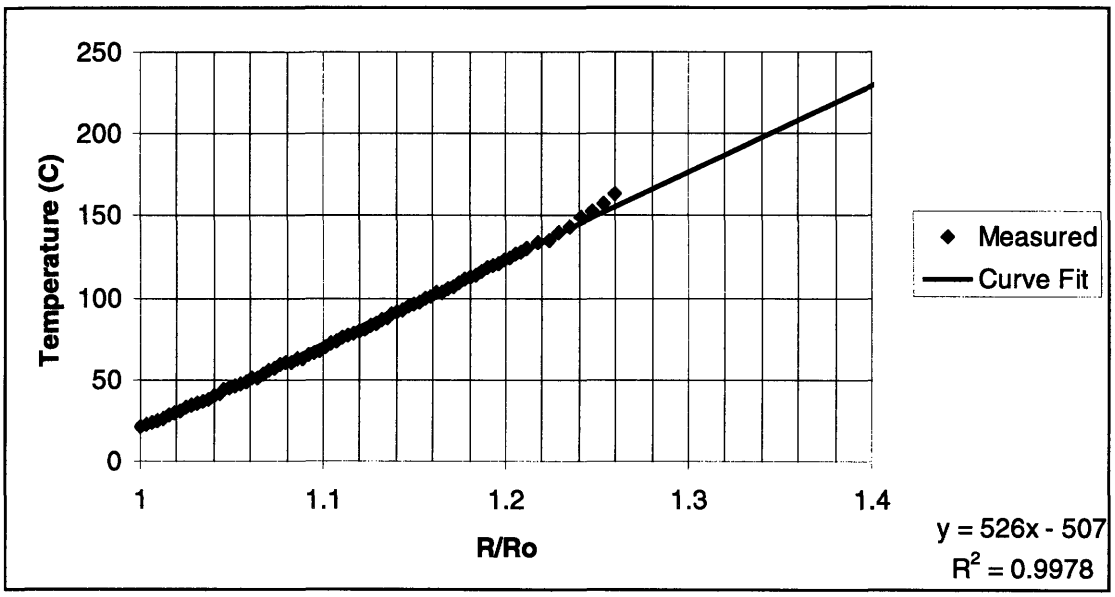

Figure 5.1 Results of temperature-resistance measurement for platinum resistor.

Using the cross-sectional area of the resistors, which is now known to reasonable accuracy, the maximum current before electromigration may be calculated. As discussed in Chapter 3, the maximum current density before electromigration is $9x10^6$ A/cm^2. Using this we can calculate the maximum current for each resistor. The results of this are shown in Table 5.2.

	Resistor #	Computed Line Width (um)	Maximum Current (mA)
Slide 1	1	8.3	71.3
	2	8.4	71.7
	3	7.7	65.5
	4	8.2	69.9
	5	10.4	89.1
	6	8.4	72.1
	7	8.4	72.1
	8	10.9	93.2
Slide 3	1	10.0	85.6
	2	9.7	83.2
	3	5.7	49.1
	4	5.9	50.6
	5	9.0	76.7
	6	9.1	78.2
	7	9.5	80.8
	8	10.5	89.8

Table 5.2 Computed electromigration limits for resistors.

These results are used as guidelines during testing of microbubble devices to avoid burning out the resistors.

5.2 Resistor Testing

The main objective for the resistors was that they be able to reach high enough temperatures to boil water. The resistors were tested on a probe station using an HP4145b to vary the voltage and measure the resulting current through the resistor. A PDMS gasket was placed on top of the slide and filled with water. The gasket contained the water and kept it from touching the electrical contacts and probes. Figure 5.2 is a schematic of this configuration.

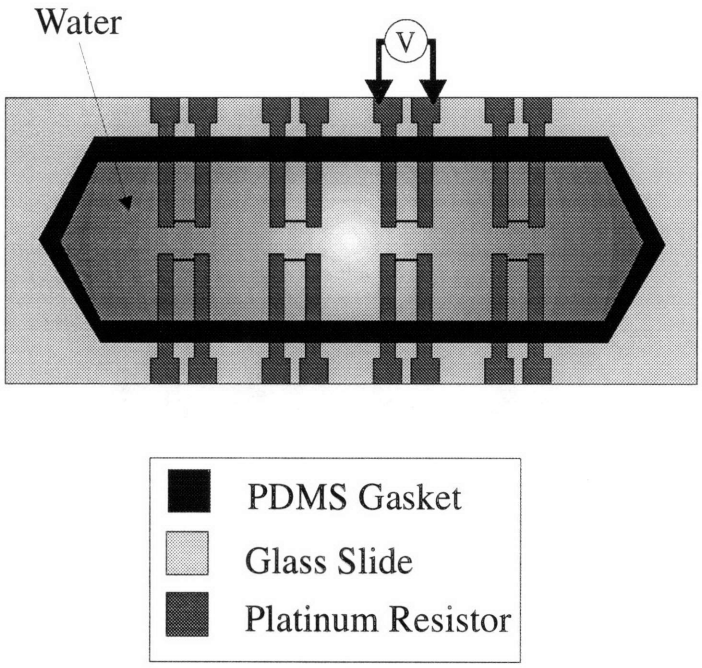

Figure 5.2 Resistor test configuration.

5.2.1 Electrolysis

Upon ramping the voltage across resistors from zero to about 20-30 V, there was violent bubbling originating not from the hot part of the resistor, but from the edges of the wide connector lines. It was evident that the bubbles were gas bubbles and not water vapor bubbles because the bubbles did not condense when the heater was turned off. Some bubbles did, however, decrease in size slightly, probably due to a small amount of water vapor condensing. There were two theories for the formation of gas bubbles, instead of vapor bubbles. One possibility was that gas dissolved in the water or the glass slide was coming out of solution, since the solubility of air in water decreases with increased temperature. The other possibility was that electrolysis of the water was occurring and the water was being broken down into hydrogen and oxygen.

To test whether electrolysis was taking place, probes were contacted to non-connected lines as shown in Figure 5.3.

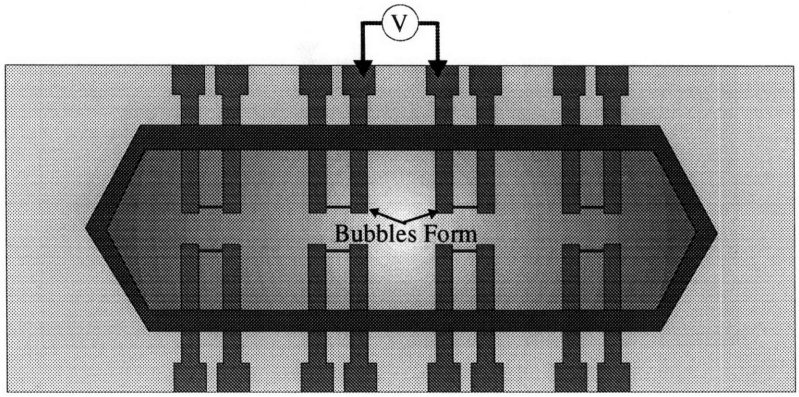

Figure 5.3 Electrolysis test: Applying voltage across unconnected lines resulted in bubbling for the same voltages that resulting in bubbling on resistors.

When the same range of voltages were applied across these unconnected lines as were applied to resistors, bubbling resulted. Larger bubbles would form and stick to the anode, and smaller bubbles would form at the cathode and quickly float away. When the anode and cathode were reversed, the bubbling phenomenon was reversed as well. It is assumed that the larger bubbles were oxygen and the smaller, lighter bubbles were hydrogen. This experiment supported that electrolysis was occuring.

In order to eliminate the electrolysis, the current through the water needed to be reduced. Two ways of doing this are to lower the conductivity of the water or to insulate the metal lines. Initially the latter solution was explored.

In order to insulate the platinum resistors, many different methods were attempted. First the slide was coated with silicon dioxide using PECVD (plasma-enhanced chemical vapor deposition). This did not prove to be an effective means of insulation because the oxide did not adhere well to the platinum, and cracked off. Solvents and acids were then used to clean the slides, in case the adherance problem was caused by a dirty surface, but the oxide still would not stay on the platinum. Next a new insulating material was used. Polyimide was spin coated on the slides, but proved to be even more problematic than the oxide. The polyimide did not coat the slides evenly and peeled off of the resistors. Finally, new slides were fabricated with an extra 100Å layer of titanium on top of the platinum. This acted as an adhesion layer, and the oxide did not come off of the resistors when deposited in the PECVD. However, when the resistors

were tested in water as before, cracks in the edges of the oxide became evident and electrolysis bubbles came through the openings.

Having little success with insulating the resistors, the conductivity of the water was examined. Deionized water was used exclusively for the testing so it seemed that electrolysis should not be able to occur. After flushing the slides, gaskets, and glassware for several minutes with deionized water, and testing again, the problem of electrolysis was eliminated.

5.2.2 Dissolved Gas

At this point the resistors were tested once again using the HP4145b to ramp the voltage and measure the current. As the voltage is increased, the current through the resistors increases and they heat up due to ohmic heating. Without the effect of electrolysis, bubbles were formed on the resistor when it reached high enough temperatures. When the power was turned off, however, it was evident that some gas was present in the bubbles. Although the bubbles got smaller without the heat, they did not completely condense. This was thought to be caused by dissolved gas in the water and slide coming out of solution.

To remedy this, deionized water was boiled on a hotplate before being used in the heater testing. Boiling the water should have removed most of the dissolved air, since the solubility of air in water decreases with increasing temperature. Upon testing the resistors with the boiled water, however, there were still non-vapor bubbles present.

It was thought that these bubbles were probably created from gas dissolved in the glass slide or platinum resistors. In order to remove the gas from the slide before testing, it would be necessary to heat the resistors in a vacuum environment. This was not attempted, however, because a vacuum bake oven was not available.

The boiled, deionized water was once again used to test the resistors, but this time the delay time for the ramping of voltage was specified to be 1ms, significantly shorter than the default value for the HP4145b. The delay time is defined as the amount of time the resistor is left at a particular voltage before a measurement is made. Also, the voltage was ramped up to a lower value, just sufficient to form bubbles for a given resistor.

When resistors were tested in this way, smaller bubbles formed on the metal line and disappeared completely within several seconds of the power being turned off. For these conditions, it is expected that pure vapor bubbles were formed on the resistors. Thus, since bubbles were formed with a delay of 1ms, the time constant of bubble formation must be less than 1ms, confirming the validity of this assumption in Chapter 2.

5.3 I-V Characteristics

Using an HP4145b, I-V measurements were performed on several resistors under various conditions. The voltage was varied, and the resulting current was measured.

As the current flowing through the resistors increases, they heat up due to ohmic heating. Additionally, as characterized above, the resistance of the resistors increases with temperature. Consequently, the I-V curves were not straight lines, since the resistance is not constant with temperature, and the inverse slope of the curve is equal to the resistance. As the resistor gets hotter, the slope of the I-V curve changes more quickly.

In addition to the amount of current flowing through the resistor, the amount of heat dissipation from it also affects the heater temperature. As discussed in Chapter 2, the amount of heat dissipated is a function mainly of the conduction down into the glass slide and conduction into the medium above the resistor. In the following sections, results will be shown for resistors tested in air and water.

5.3.1 Air

First the resistors were tested in air. The thermal conductivity of air is over an order of magnitude less than that of water. Consequently, one can expect that the heat dissipation from the resistor to the air would be significantly less than that for water. Thus, the heating of the resistor will be greater in air than in water, resulting in a higher resistance for a given current.

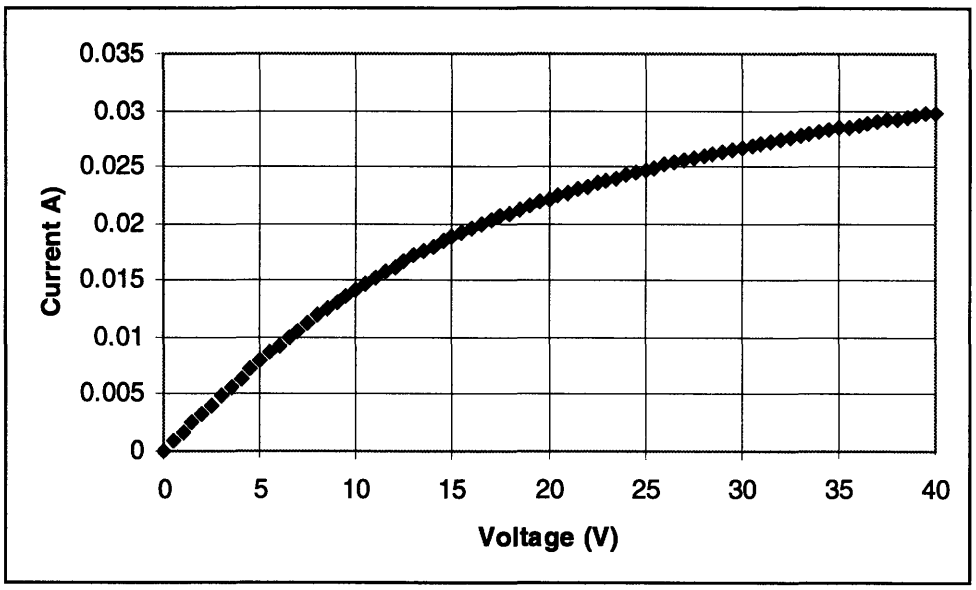

Figure 5.4 I-V curve measured in air (Slide 3 Resistor 1).

A typical I-V curve for a resistor measured in air is shown in Figure 5.4. The curved shape is caused by the elevated resistance as the resistor gets hot.

5.3.2 Electromigration

In testing the resistors, it was necessary to limit the maximum current in order to avoid electromigration. The limits were calculated in Section 5.1. Initially, in testing the resistors, the maximum current was limited to approximately half of the electromigration limit; however, some resistors still were destroyed due to electromigration. An I-V curve of a resistor undergoing electromigration is shown in Figure 5.5.

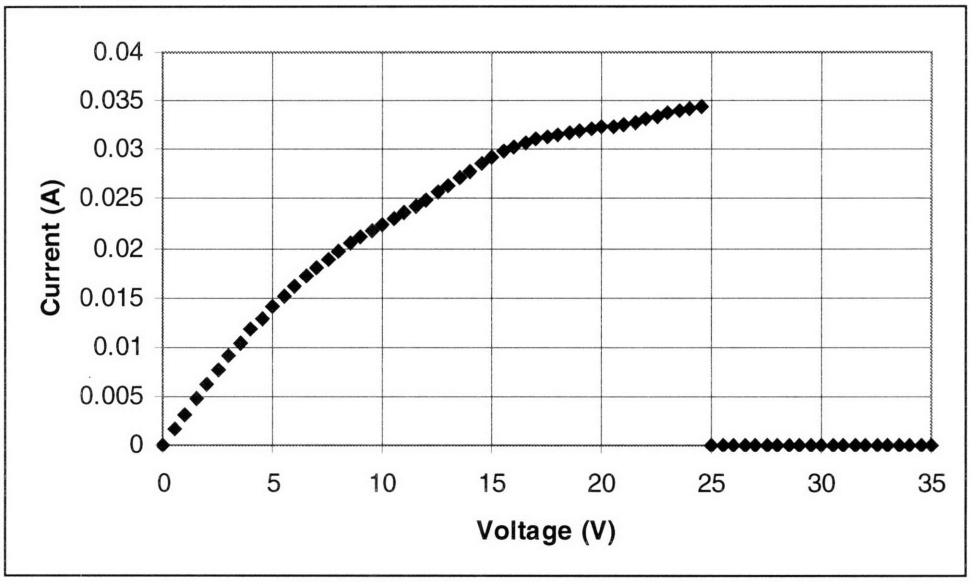

Figure 5.5 I-V curve of a resistor exceeding the electromigration limit (Slide 3 Resistor 5).

A photograph of a resistor destroyed by electromigration is shown in Figure 5.6.

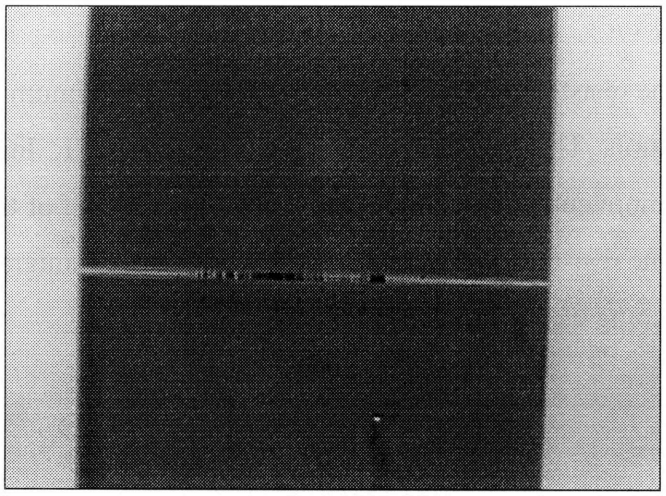

Figure 5.6 A resistor after electromigration.

It is thought that the resistors were destroyed beneath the electromigration limit because the elevated temperature of the resistors makes it easier for electromigration to occur, resulting in electromigration at a lower current density than predicted.

5.3.3 *Electrolysis*

As described above, when the resistors were first tested in water, violent bubbling due to the electrolytic breakdown of water occurred before boiling was observed. As the bubbles originated on the wide contact lines instead of the heating element, it follows that the heat dissipation of the resistors was not effected by the gas bubbles.

An I-V curve of a heater tested in water with electrolysis (no boiling) occurring is shown in Figure 5.7. Also plotted is the same resistor tested in air to show the difference in resistance of the heater resulting from the increased heat dissipation in water.

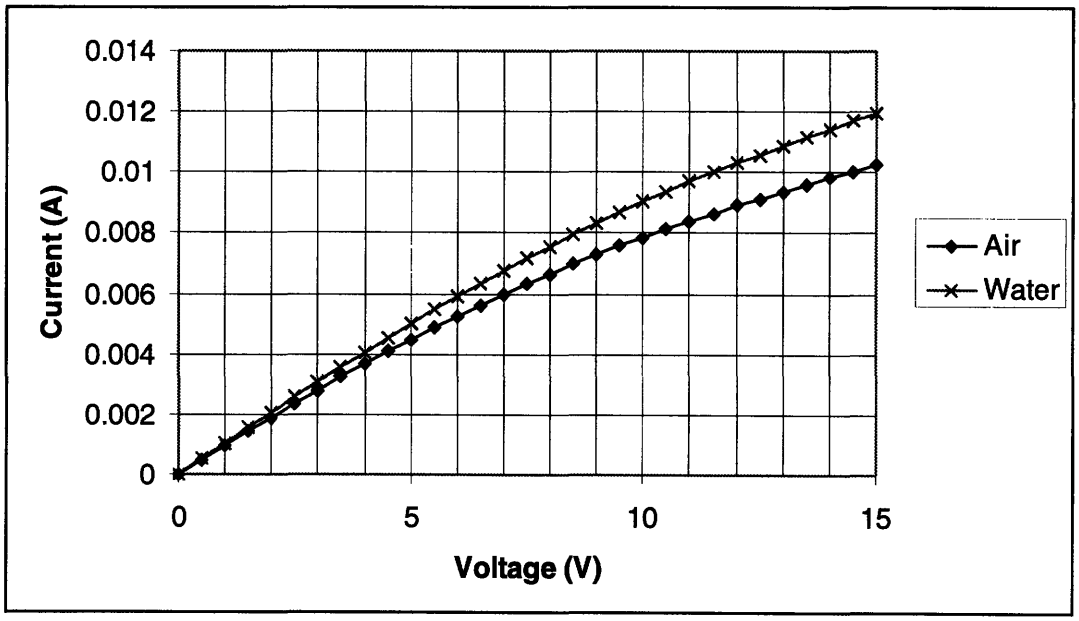

Figure 5.7 I-V curve of resistor tested in water with electrolysis, and in air (Slide 1 Resistor 4).

This curve shows that the resistance of the heater when tested in air is higher than when it is tested in water, resulting in a lower current for a given voltage. This higher resistance for a given voltage represents a higher temperature for a given voltage and thus demonstrates that there is less heat dissipation in air than in water, as expected.

5.3.4 *Boiling*

When the problem of electrolysis was eliminated, the resistors were once again tested in water. When the resistor reached a sufficient temperature, boiling occurred

along the length of the heater. After the power was turned off, small air bubbles remained on the resistor due to the dissolved gas coming out of solution, as described previously. In subsequent tests, the air bubbles served as nucleation sites for boiling, the inception of boiling occurred at a much lower temperature.

Photographs of bubbles forming on a long and short line resistor are shown in Figure 5.8 and Figure 5.9.

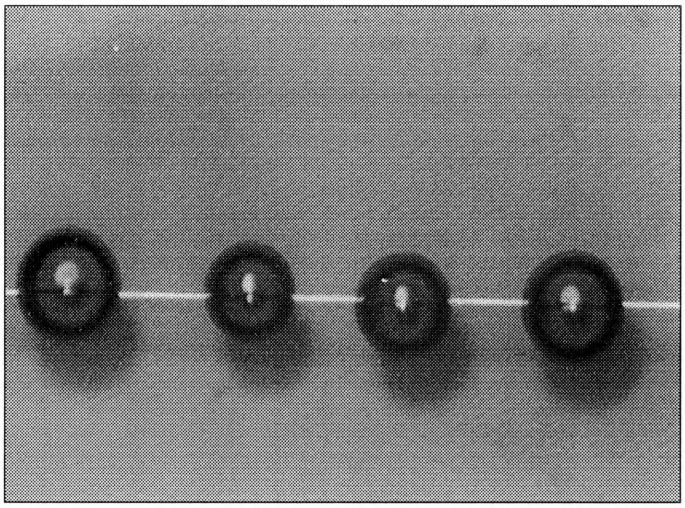

Figure 5.8 Bubbles forming on a long line resistor during boiling.

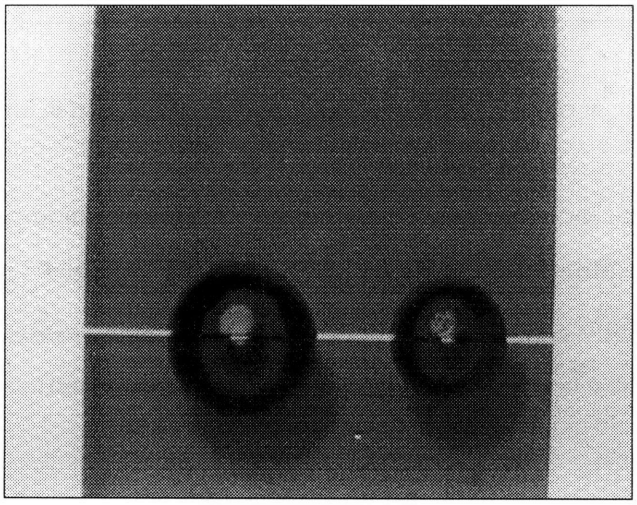

Figure 5.9 Bubbles forming on a short line resistor during boiling.

When boiling begins and bubbles form on the resistor, the heat dissipation into the water increases drastically. This is a favorable phenomenon for the operation of the device because the onset of boiling is represented as a sharp increase in current on the I-V curve. This is because when the heat dissipation increases, the temperature decreases, resulting in a lower resistance and thus a higher current through the resistor. An I-V curve for the onset of boiling on a line resistor is shown in
Figure 5.10.

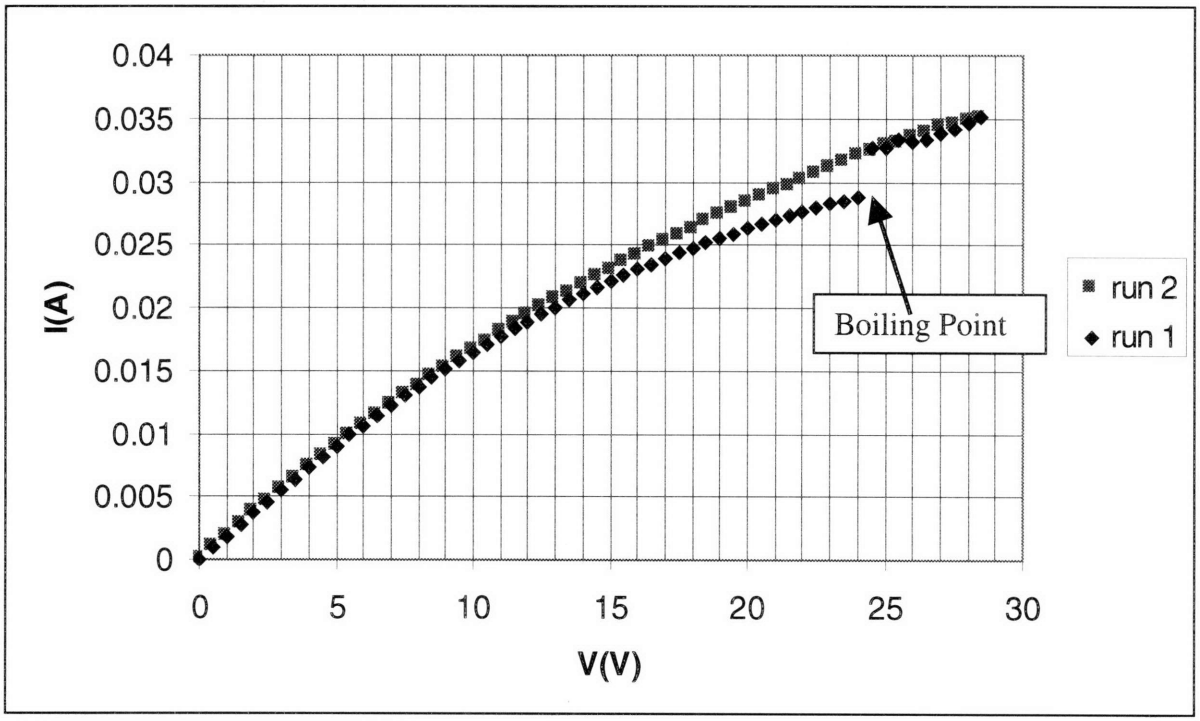

Figure 5.10 I-V curve in water, run 1 is the inception of boiling; run 2 uses the residual gas bubbles to nucleate bubbles at a lower temperature (Slide 3 Resistor 2).

In this I-V curve we can see that for the first run when no bubbles were present on the line, there is a sharp jump in current at the onset of boiling. For the second run, residual bubbles are left on the heater and serve as nucleation sites for boiling resulting in a smooth I-V curve with boiling beginning at a lower temperature. The two curves are very close after the boiling begins for run 1.

In later tests, when no dissolved gas came out of solution, the jump in the I-V curve occurred during each heating cycle for the resistors, since there were no residual air bubbles left when the power was turned off.

Using the calibration given in Figure 5.1 for the temperature-resistance relationship of the resistor, we can plot the temperature of the resistor for each current and find the boiling temperature. The current vs. temperature plot corresponding to the I-V curve shown above is in Figure 5.11. On this plot we can see that water boils at approximately 308°C, at which point the temperature drops rapidly due to the increased convective heat transfer associated with boiling.

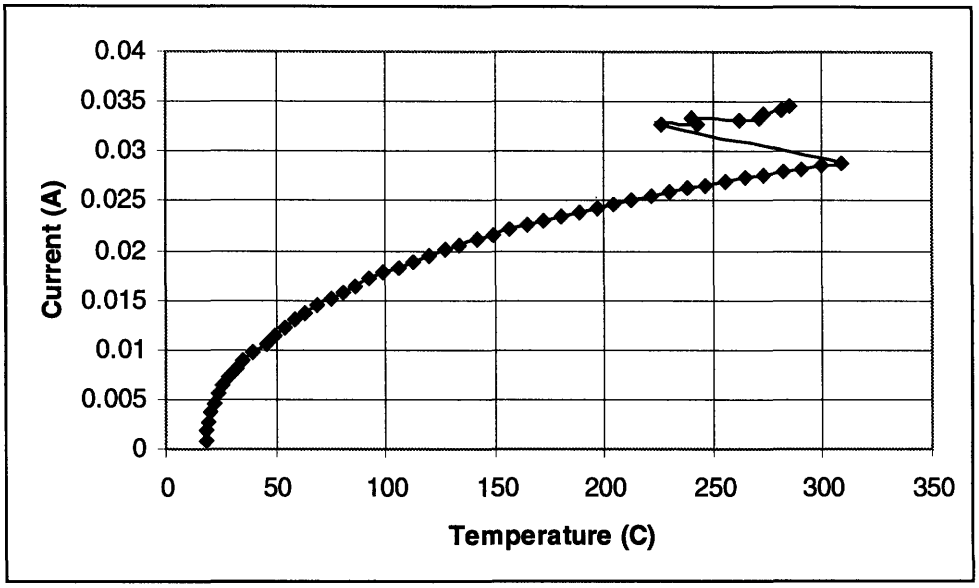

Figure 5.11 Plot of current vs. temperature; the sharp change is onset of boiling (Slide 3 Resistor 2).

The boiling points for the 5 resistors tested ranged from 250°C to 308°C. The lowest calculated value for the superheat limit of water was found to be 273°C (Chapter 2), so these measured boiling points suggest that the bubble nucleation occurs either in the homogeneous regime, or by a weak heterogeneous mechanism.

In the subsequent testing of the fully-assembled device, at which point the resistor is no longer visible, we will use the jump in the I-V curve to determine when a bubble is formed and verify that the bubble creates a jet of water out of the channel to eject a particle.

5.3.5 *Comparison to the One-Dimensional Model*

At this point we may determine the validity of the one-dimensional heat transfer model developed in Chapter 2. By programming the HP4145b to apply a specified current to a resistor for a given time, and then calculating the resistance at that point, we may determine the temperature of the resistor for a given time. Unfortunately, the minimum delay time possible on the HP4145b is 1ms, so measurements for smaller times could not be completed. The results of this test are shown in Figure 5.12. For a time of 1ms, the experimental temperature is 33.2°C compared with the 42.7°C predicted by theory. However, at 10ms, the theoretical and experimental values diverge dramatically. From this we can see that the one-dimensional semi-infinite approximation is not a very useful approximation for times greater than 1ms.

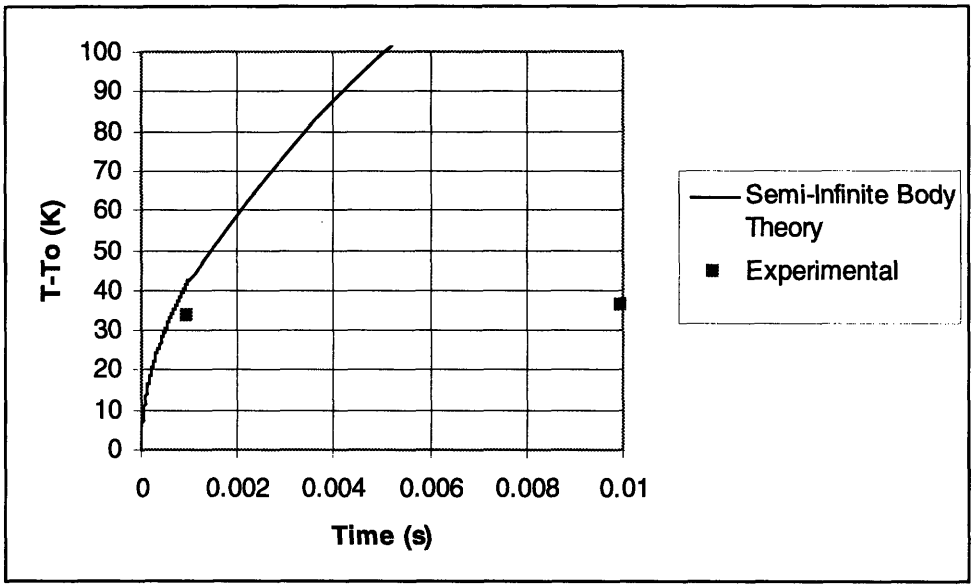

Figure 5.12 Comparison of experimental results with semi-infinite body theory.

5.4 Second Generation Resistor Testing

After a considerable amount of testing of the resistors characterized above, a drift in the boiling temperature became apparent. In order to determine the reason for this, the resistors were recalibrated as described in Section 5.1. The temperature versus normalized resistance curve is shown in Figure 5.13.

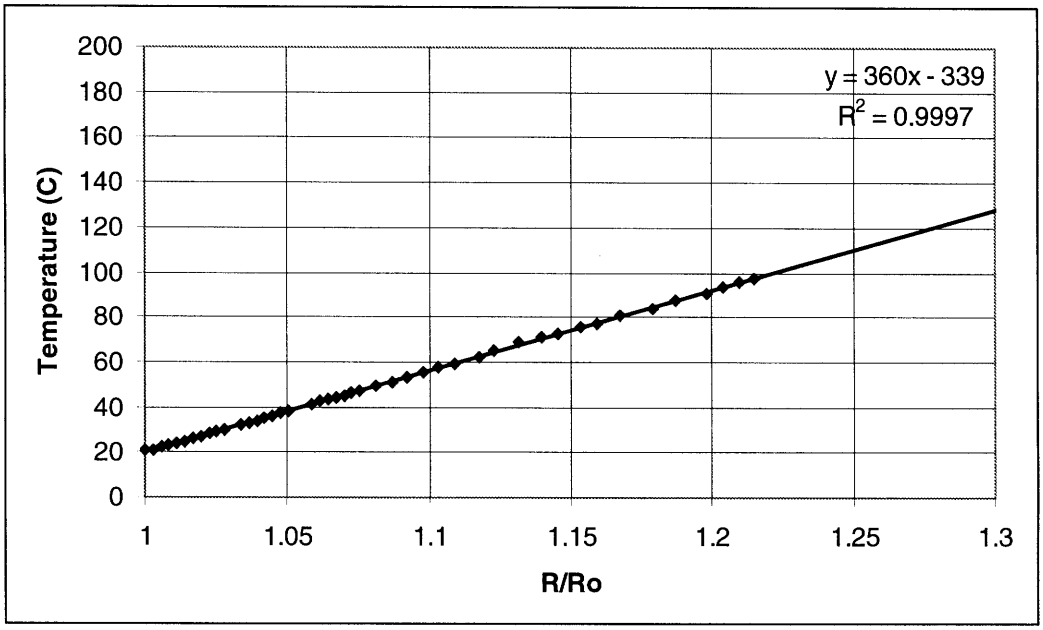

Figure 5.13 Recalibration of resistors after testing.

The dramatic change in temperature-resistance characterization led to the testing of a second generation of resistors. It is thought that these changed characteristics are caused over time by the heating of the resistors. The operation of the resistors effectively causes them to anneal themselves. Annealing changes the geography of the platinum grain boundaries and thus changes the resistivity of the resistors.

In order to avoid this effect in future testing, new resistor slides were annealed at 600°C for 1 hour as the last step in their process. This temperature is higher than operating temperatures are likely to reach, but not so high that major agglomeration will result (see Chapter 2). Once the anneal was complete, the new resistors were characterized as described above for the first generation resistors.

5.4.1 Resistor Characterization

First, the resistivity of the platinum at room temperature was found to be $2.056 \times 10^{-7} \Omega m$, less than the unannealed resistors that were $2.41 \times 10^{-7} \Omega m$. Next the resistances were measured using a multimeter, and the line widths were computed as before, as shown in Table 5.3.

	Resistor #	L (um)	R (Ohms)	Computed Line Width (um)	Design (um)
Slide 3	1	3000	553	13.12	6
	2	2500	481	12.57	6
	3	500	146	8.28	3
	4	1000	281	8.61	3
	5	1000	205	11.80	6
	6	2000	409	11.83	6
	7	1500	310	11.70	6
	8	1000	186	13.00	6

Table 5.3 Measured resistances and computed line widths of second generation resistors.

The temperature-resistance characteristic or the resistors was then measured on a hotplate as described above. The new calibration is shown in Figure 5.14.

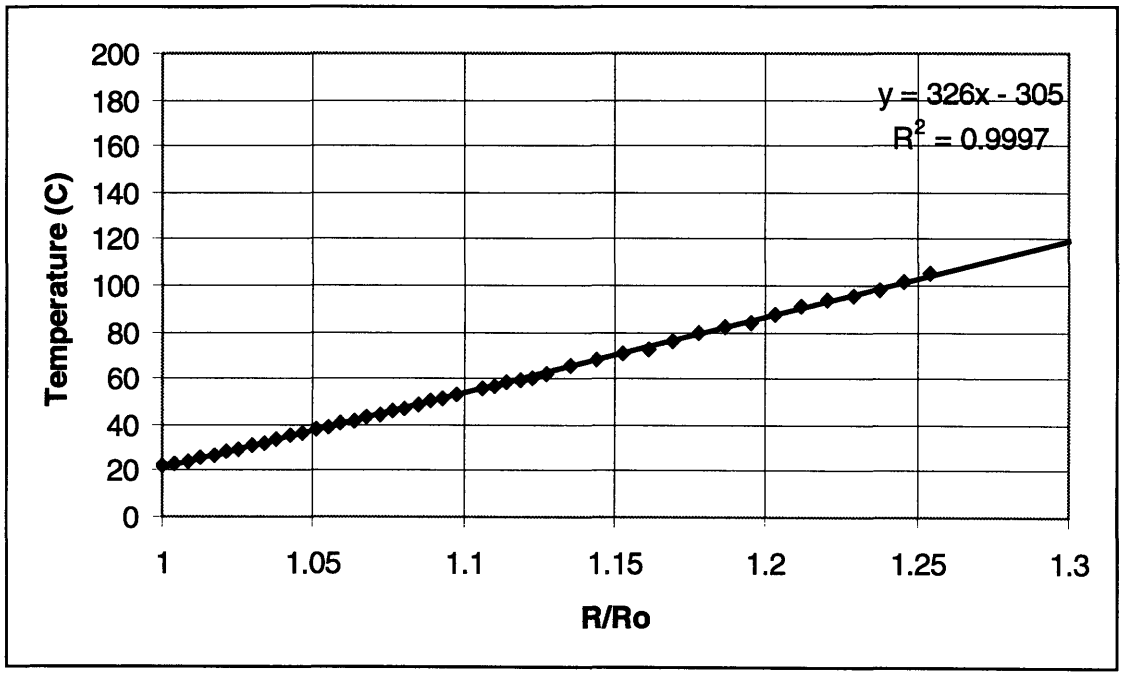

Figure 5.14 Temperature-resistance calibration of annealed platinum resistors.

This calibration should remain accurate since the normal operating temperatures of the resistors do not exceed 400°C.

5.4.2 Comparison to the Theoretical Model

As done above, measurements were taken at short times to explore the validity of the semi-infinite body approximation. 5 Volt pulses with durations ranging from 1ms to

1 second were applied to the resistors and the resulting temperatures were computed using the calibration shown above. At 1 ms the predicted temperature difference was 96°C while the measured temperature difference was 37°C. This suggests that the semi-infinite body theory is not accurate for times at or above 1ms. Unfortunately, the equipment was not capable of measuring for shorter times than 1ms. The results of this test are shown in Figure 5.15 and the measurements over a longer time range are shown in Figure 5.16.

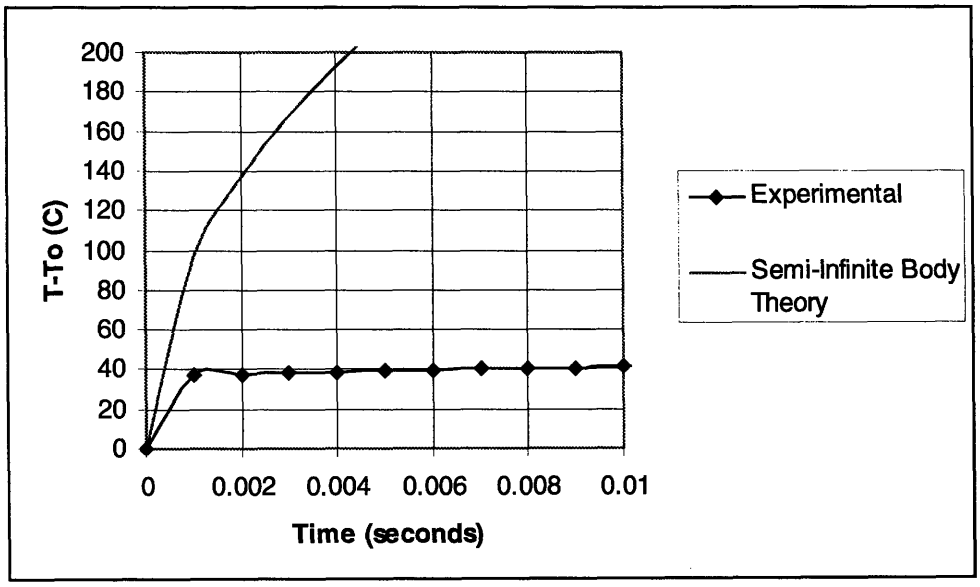

Figure 5.15 Comparison of theoretical predictions and measured results for 2nd generation resistors.

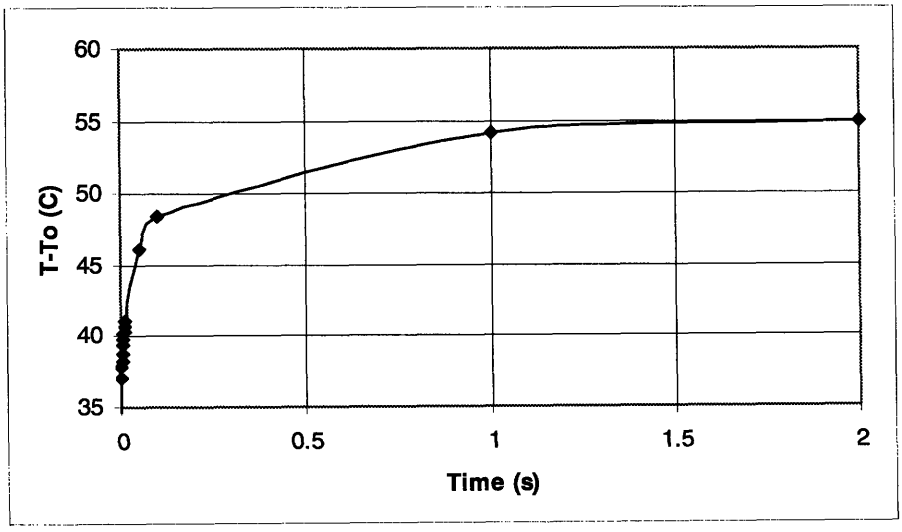

Figure 5.16 Full measured results.

One reason for the inaccuracy of the approximation is that one-dimensional conduction, rather than three-dimensional conduction was assumed. Also, the heat capacity and properties of the resistor between the water and the glass were not taken into account.

5.4.3 Boiling

At this point, the bubble formation characteristics of the resistors were tested as described previously with boiled, deionized water. Voltages were ramped up by 0.5V steps with delay times of 1ms using the HP4145b, as before. None of these tests resulted in residual gas bubbles since the delay time was short, and the maximum voltage used was just above the bubble nucleation voltage, determined by testing. All resulting vapor bubbles condensed back into the liquid phase within one minute of stop of current flow.

A resulting I-V curve is shown in Figure 5.17, and the corresponding temperature curve is shown in Figure 5.18.

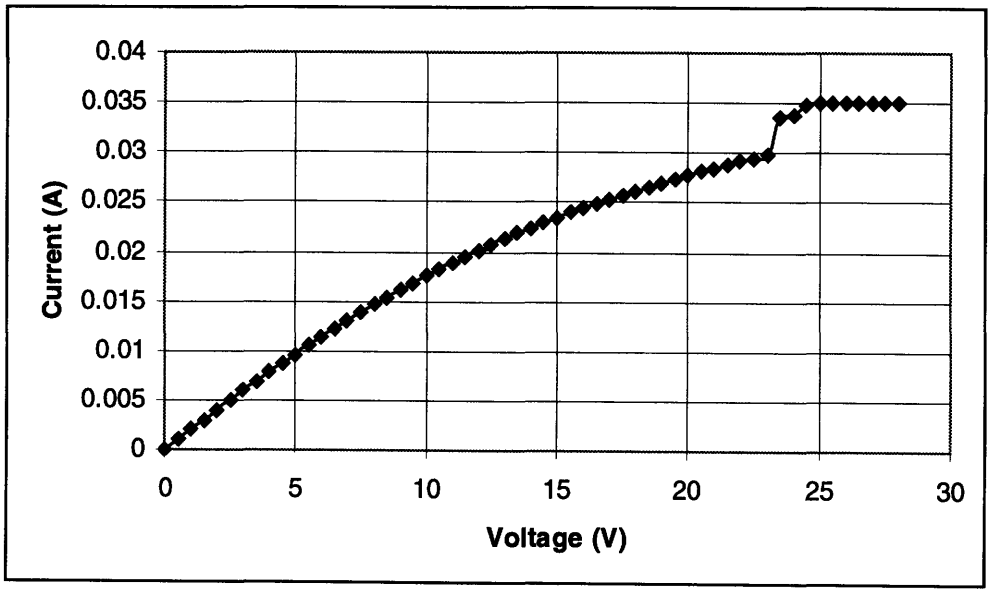

Figure 5.17 I-V curve of a 2nd generation resistor during the onset of boiling (Slide 3 Resistor 2).

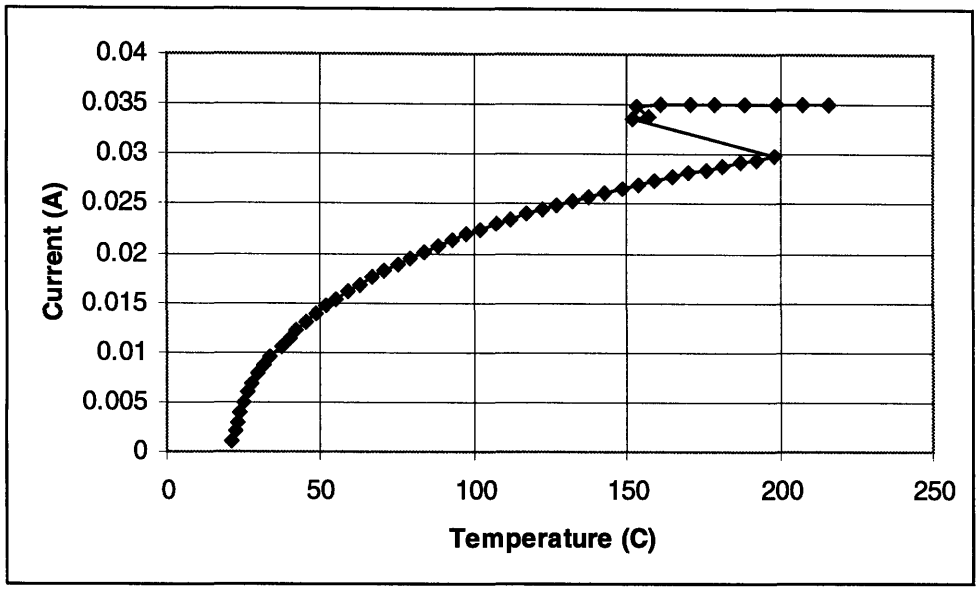

Figure 5.18 Corresponding current vs. temperature curve (Slide 3 Resistor 2).

From the curve we can see that the onset of boiling occurred at about 200°C, a much lower temperature than for the first generation resistors, and well below the superheat limit of water. For the 8 second generation resistors tested, boiling points ranged from 128°C-200°C, with the majority of the temperatures above 180°C. This suggests that the boiling is in the heterogeneous nucleation regime as discussed in Chapter 2. The cavity radii corresponding to these boiling inception temperatures are calculated from Equation (5-2).

$$r_c = \frac{2\sigma T_{sat}}{h_{fg}\rho_v(T_w - T_{sat})} \qquad (5\text{-}2)$$

The results of this calculation are shown in Table 5.4.

Resistor #	Boiling Temperature (C)	Cavity Radius (um)
1	200.7	0.33
2	198.3	0.34
3	170.4	0.47
4	183.2	0.40
5	128	1.19
6	188	0.38
7	189	0.37
8	169	0.48

Table 5.4 Bubble nucleation cavity radii corresponding to measured boiling temperatures.

From this we can see that bubbles were nucleated in radii ranging from 0.3-1.2μm. As discussed in Chapter 2, these cavities were most likely formed during the 600°C anneal, during which the grooves at the grain boundaries widened creating cavities.

5.4.4 Repeated Testing

The second generation resistors were also tested for the repeatability of their boiling temperatures. I-V curves were measured as in the previous section, and then remeasured for the same conditions several times. Between measurements, time was given for the vapor bubbles to dissipate so that the characteristic jump in the I-V curve at boiling could be observed with each measurement. The boiling point was found to be very repeatable, and an example of the results is shown in Figure 5.19.

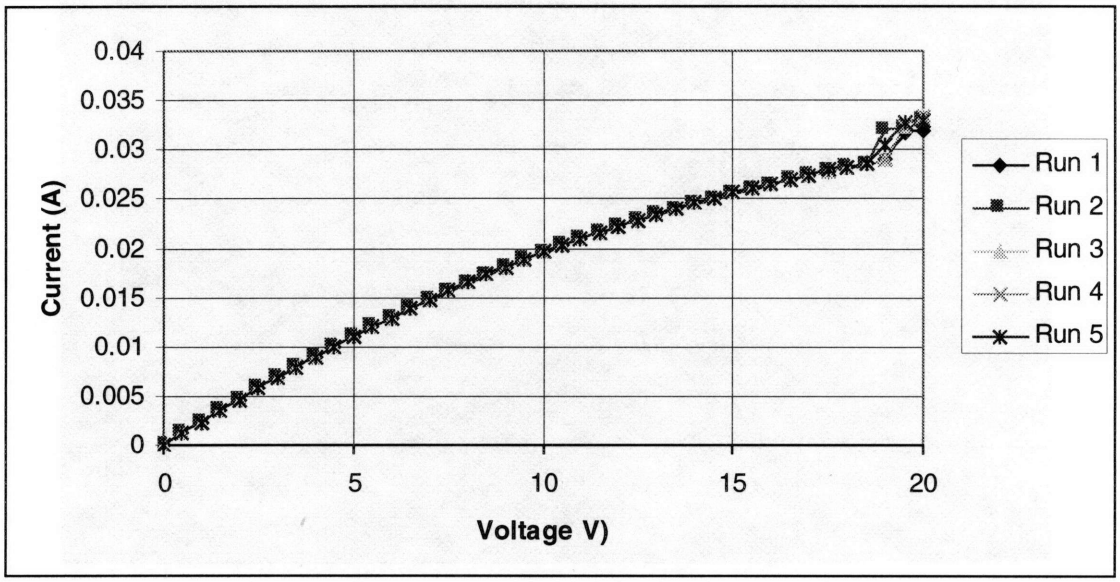

Figure 5.19 Repeated boiling tests on a 2nd generation resistor (Slide 3 Resistor 6).

This result demonstrates the potential of a control system based on a jump in the I-V curve at the onset of boiling, since the boiling point remains fixed.

Another interesting result from this testing is that for a particular resistor, the bubbles tended to nucleate in the same locations on the resistor each time. This strengthens the hypothesis that the bubbles are nucleating in the heterogeneous regime, in cavities created by thermal grooving caused by the anneal

5.4.5 *Cavity Size Before and After Anneal*

In order to test the hypothesis that cavities are grown during the anneal, SEM photos were taken of the platinum film before and after the anneal was performed. Figure 5.20 shows an SEM of a platinum film which has not been annealed. From this picture, we can see that the maximum void diameter is about 0.45μm, a radius of about 0.22μm. These voids are likely caused by pinholes in the film from the deposition process.

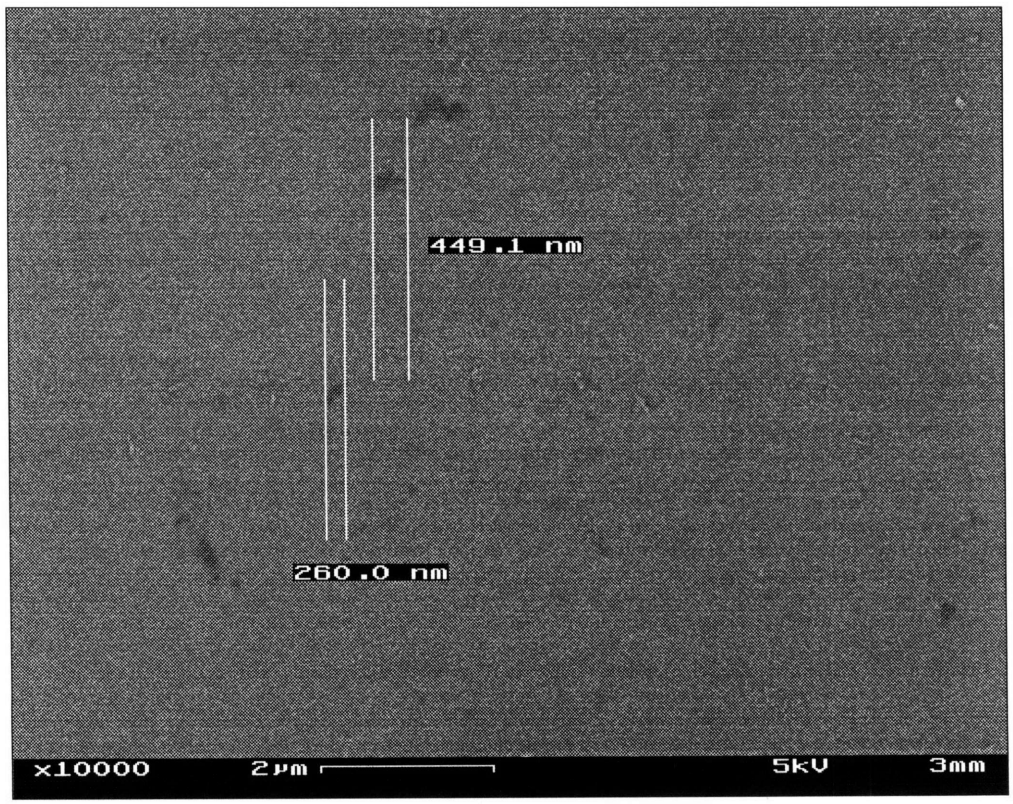

Figure 5.20 SEM of unannealed platinum film, with sizes of voids.

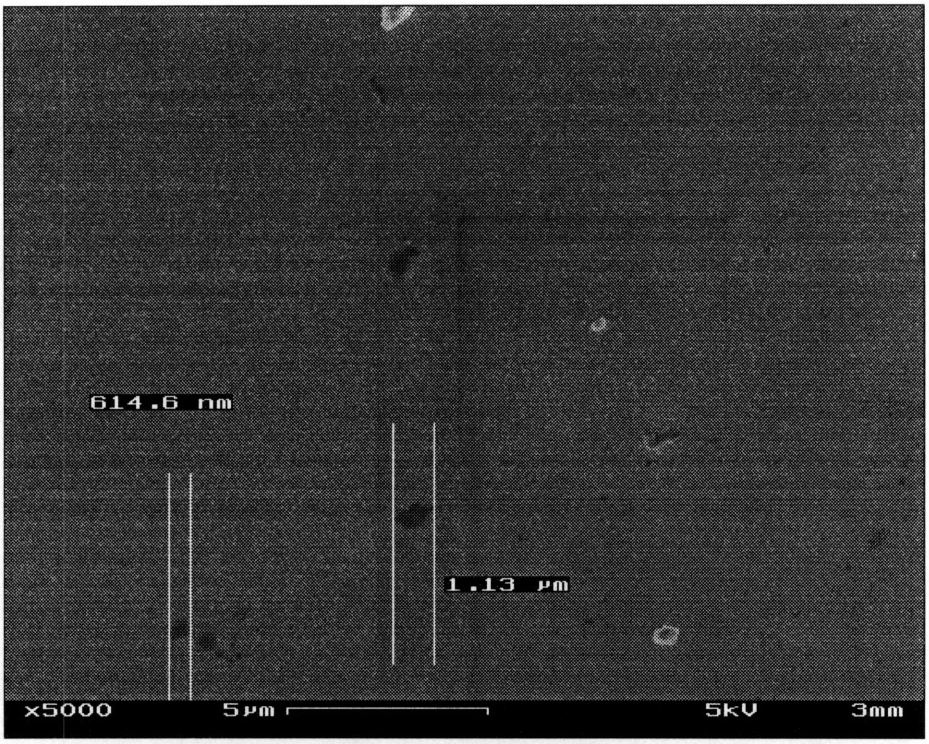

Figure 5.21 SEM of annealed platinum film.

An SEM of the film after the anneal is shown in Figure 5.21. From this we can see that the maximum hole diameters are bigger than on the unannealed platinum, about 1.1µm diameter. Although these holes were also probably started as pinholes in the film, the anneal made the holes bigger, and thus created better nucleation sites for bubbles.

Another effect of the anneal is that the grains of the metal tend to grow. This is shown in Figure 5.22 and Figure 5.23. The grains are obviously much larger in the annealed platinum film. This also makes sense given that the resistivity of the annealed platinum is lower than the anannealed platinum. The resistivity should be lower if the grains are longer since the current travels through grains more easily than it does through grain boundaries.

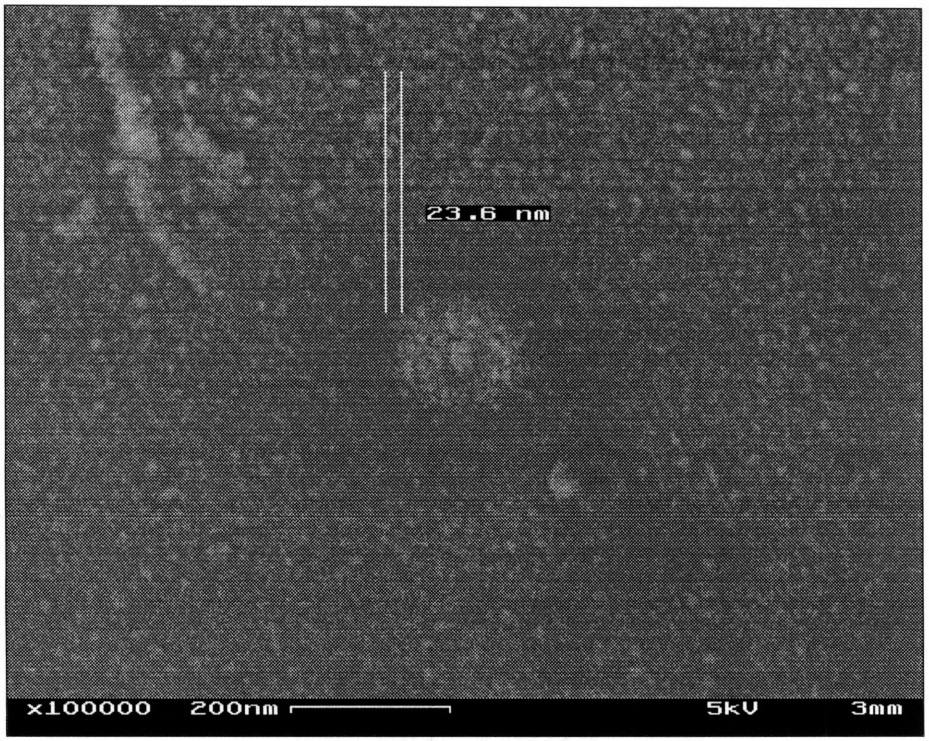

Figure 5.22 SEM of grains in unannealed platinum.

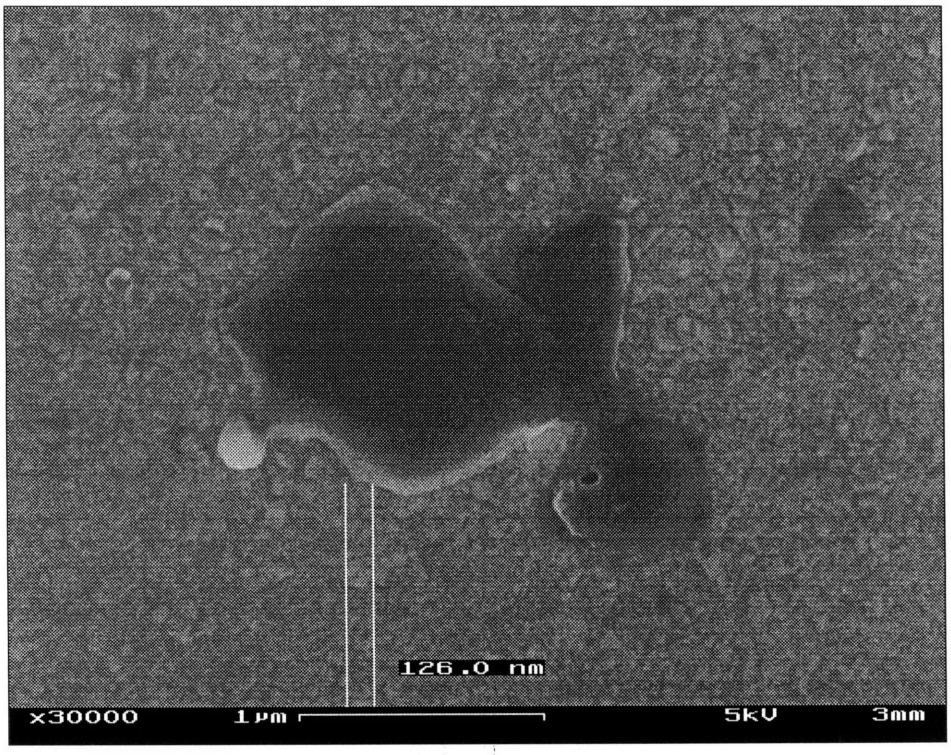

Figure 5.23 SEM of grains in annealed platinum.

5.5 Complete Device

The cell chip was attached to the glass resistor slide as described in Chapter 4, and then tested in two ways. First tests were done with stagnant fluid on the device. Then the device was put into the flow chamber (described in Chapter 3) for testing. The results of these tests are described below.

5.5.1 Static Tests

For these tests, several drops of bulk solution were placed on top of the cell chip, and contained by the PDMS gasket. A drop of the polystyrene bead solution was then added to the bulk fluid and allowed to settle. The bulk solution was a 0.05% solution of Triton x-100 surfactant in deionized water. The bead solution was about 1% beads diluted in the same bulk solution. Some of the beads settled into wells, as shown in Figure 5.24. When voltage across the resistor was ramped up by the HP4145b, an I-V curve with a jump similar to that in Figure 5.10 was produced, demonstrating that boiling had occurred. Consequently, the bubble formation under the well caused a volume expansion which rapidly ejected the beads from the well. Figure 5.24, Figure 5.25, and Figure 5.26 show this process. First the beads are in the well, and then they are rapidly expelled.

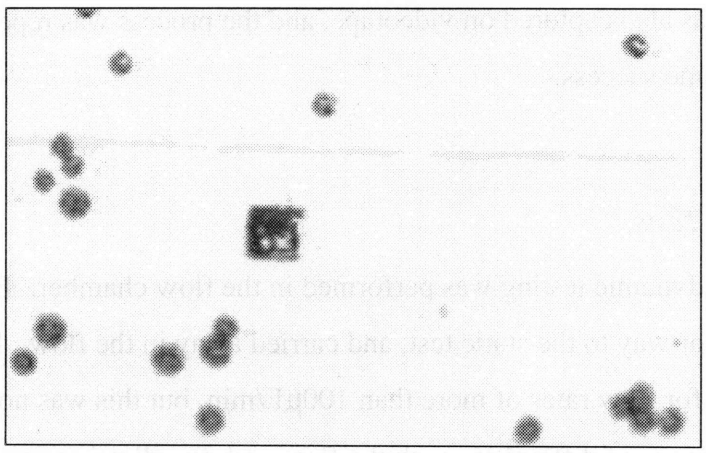

Figure 5.24 The beads are settled into the well.

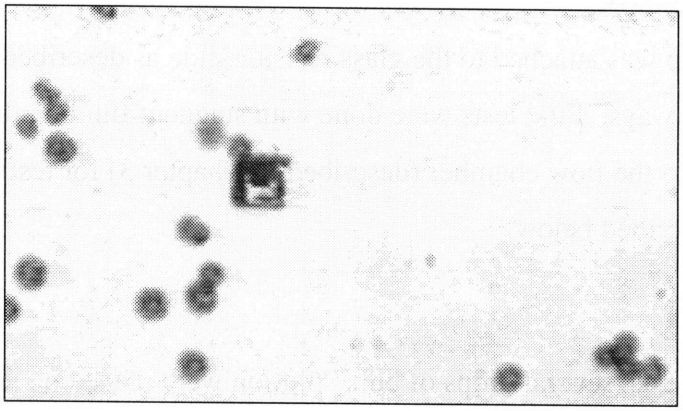

Figure 5.25 The jet of water from inside the well has ejected the beads.

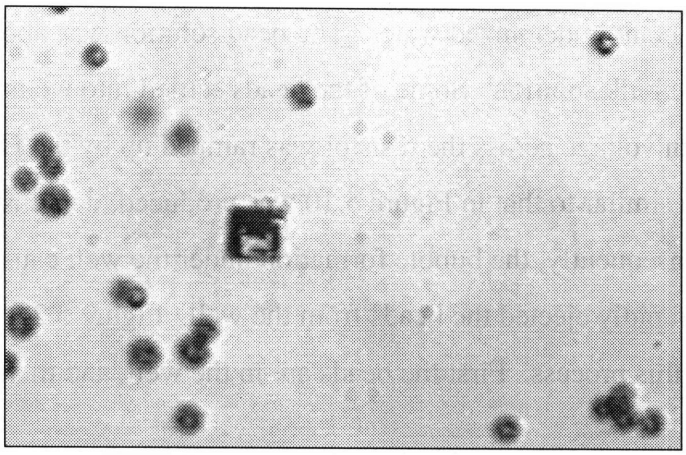

Figure 5.26 The well is now empty and the beads flow away.

This sequence was also captured on videotape, and the process was repeated multiple times with the same success.

5.5.2 Dynamic Tests

Preliminary dynamic testing was performed in the flow chamber. Beads were ejected in a similar way to the static test, and carried away in the flow. Beads remained held in the wells for flow rates of more than 100μL/min, but this was not fully characterized because of difficulties with the flow and visualization equipment. Regardless, the preliminary tests suggested that the beads are held in the wells against a reasonable flow rate, and are ejected into the flow when a microbubble forms.

6 CONCLUSION

In this work, a microbubble-powered cell actuator has been designed, fabricated, and tested. The goal of releasing a spherical particle, on demand, from a silicon well using vapor bubble actuation has been realized. What follows is a discussion of the results and of the potential for future work.

6.1 Discussion

In characterizing the platinum line resistors, many issues were addressed in order to achieve optimal performance. The problem of the electrolytic decomposition of water, a problem also reported by Lin et al. [20, 28] for their line resistor experiments involving water, was eliminated by flushing all glassware and chips with deionized water before use. This way, the water was not conductive enough to allow electrolysis to occur. For later testing, an insulation scheme for the resistors must be developed.

The problem of residual gas bubbles left on the line resistors after the power was turned off was avoided by using a small delay time (1ms) between steps in the IV curve and ramping up to a voltage just above that necessary to induce boiling. This suggests that either dissolved gas takes longer than 1ms to come out of solution and is a slower process than boiling, or that the bubbles resulting from boiling have some dissolved gas in them, but are small enough for the gas to redissolve back into the solution rapidly. Regardless, the appearance of residual gas bubbles has been eliminated in this way.

In order to have a stable calibration for the resistors, one which does not change with use, the importance of an anneal step in the process was discovered. By annealing the resistors at 600°C, a temperature well above standard operating temperatures, the problem of resistors annealing themselves during operation could be avoided. Also, the anneal resulted in a platinum film with a lower resistance due to the growth of the grains. Defects and grain boundaries in the film were also expanded during the anneal resulting in lower observed boiling temperatures, probably due to heterogeneous nucleation in the film cavities.

It was also discovered that electromigration occurs at lower current densities in heated materials, and thus, the operating procedure of keeping the current density below one third of the predicted electromigration limit was instituted.

Using the calibrated resistors, I-V curves were found to indicate the onset of boiling by a sharp jump in current flow, representing a lower resistance and thus a lower temperature due to increased heat transfer at boiling. This phenomenon was found to be repeatable, and an accurate indication of boiling. The jump in the I-V curve at boiling can be used as the basis for a powerful control scheme for the cell chips later on. Also, the temperature at the onset of boiling may be determined using the resistor's temperature/resistance calibration.

As previously demonstrated by Bousse et al. for many cells in larger wells [8-10], smaller numbers of spherical particles were demonstrated to settle into silicon micromachined wells and remain inside while fluid flowed over the top. This result suggests the potential for the capture of single cells in smaller micromachined wells.

Additionally, boiling characteristics resembling both homogeneous and heterogeneous regimes were demonstrated. It is likely that heterogeneous boiling occurred during the tests of the second generation resistors since bubbles appeared in the same locations on a particular resistor each time boiling occurred and boiling temperatures were found to be below 200°C. Homogeneous boiling possibly occurred during the testing of the first generation resistors since boiling points were calculated to be around 300°C, but this result may not be verified since the calibration of the resistors was not stable at this point.

6.2 Future Work

By proving the concept of microbubble cell actuation, the way has been opened for much further work in this field. Using this work as a starting point, new work can be done in both basic science and in the engineering of new devices. The physics of bubble formation on the microscale can be studied and modeled more fully. On the other hand, this cell capture concept may be built upon to create second generation cell devices. Subjects which may be addressed later on include the heat transfer model, cell capture, microfabrication, and use of live cells.

First of all, the heat transfer model can be greatly improved by doing a full three-dimensional transient simulation and including the effects of the onset of boiling. It would be useful to find the steady state power necessary to maintain a microbubble of a

particular size. This way, a bubble could be present in the chamber at all times, and the power could be modified in order to grow the bubble and eject a cell. By having a more accurate heat transfer model, more complex issues such as this could be explored. The boiling temperature and thus the bubble nucleation regime can also be studied in more depth.

A more efficient cell capture regime than settling may be explored and incorporated into the device. The settling of cells into wells is a passive process, and an active cell capture approach could yield faster results, eliminating the waiting time inherent in settling. For example, perhaps a collapsing bubble or some other pressure differential could provide the suction force necessary to pull a cell into a well. DEP forces (described in Chapter 1) could also be used to capture cells in known locations. The cell wells could be redesigned to be the proper size to reliably capture only single cells.

Furthermore, the microfabrication process can be improved upon by fabricating the resistors on quartz wafers instead of glass slides. This way, the silicon wafer can be anodically bonded to the glass wafer, providing a better seal and more exact alignment. With better alignment tolerances, the resistor-cell well combinations could be scaled down to a smaller size and thus more wells could be fit on a single chip. In the current design, there are only 8 cell wells on a chip, however, a scaled down device could yield chips capable of capturing 1000 cells or more on the same sized chip. This way, a large population of cells could be interrogated and sorted at once. A process to insulate the resistors could also be developed so that there is no chance of electrolysis when tests are performed using live cells in salt solution, and also to protect the platinum from the harsh wear due to boiling.

Once the cell chip is characterized and optimized, testing can begin with live cells. The polystyrene beads are a good approximation for cells since they are approximately the same size, shape, and density, however, live cells must be tested to ensure that conditions are suited to cells. Finally, the full μDAC system may be realized, complete with optical and control systems, to take dynamic responses of a large population of cells and then sort based on that data.

7 APPENDIX

7.1 Appendix A Glass Process

Glass slides

(Gold contaminated)

[TRL]

1. Piranha clean
   10min
   rinse and dry by hand
2. HMDS
3. Spin resist
   AZ5214 IR resist
   500rpm 9s
   750rpm 6s
   3000rpm 30s
4. Prebake 30min
5. Expose with mask 4
   Ksaligner2 20s
   Use nonreflective (black plastic) behind
   1 slide at a time
6. Postbake 2min on hotplate immediately
7. Flood exposure 30s immediately after
   Ksaligner1
8. Develop AZ422 MIF 60s
   Rinse and dry by hand
9. Quick Ash 2min (TRL)
10. Evaporate 100A Titanium, 1000A platinum on top of resist
    E-beam in TRL
11. Lift off using acetone

12. Ash resist

    2 min Ash, TRL

13. Anneal 1 hour at 600°C (Optional)

(Optional)

14. HMDS
15. Resist coat

    standard resist

    500rpm 6s

    750rpm 6s

    3500rpm 30s

    resist thickness: 1 μm

16. Prebake
17. Expose with mask 5

    Ksaligner2

    exposure 40s(ksaligner2)

18. Develop 90s (OOCG 934 3:2)
19. Postbake

7.2 Appendix B Silicon Process

Double side polished (DSP) wafers:

Front:

[ICL]

20. RCA Clean
21. Measure wafer thickness
22. Grow 1μm thermal oxide

    tubeB2

    recipe#G122

    (1100degree (C),

    Dry O2 20min

    Wet H20 50min

    Dry O2 20min)
23. Measure oxide thickness

[TRL]

24. HMDS
25. Resist coat

    standard resist

    500rpm 6s

    750rpm 6s

    3500rpm 30s

    resist thickness: 1 μm
26. Prebake 30min
27. Pattern oxide using mask 1 (large well)

    exposure 40s(ksaligner2)
28. Develop 90s (OOCG 934 3:2)
29. Postbake 30 min

[ICL]

30. Wet oxide etch (1 μm)

    BOE

    10 min

31. Ash resist

    Asher

    Recipe: STD (1 min)

[TRL]

32. HMDS

33. Resist coat

    standard resist

    500rpm 6s

    750rpm 6s

    3500rpm 30s

    resist thickness: 1 um

34. Prebake 10min

35. Resist coat (2^{nd} coat)

    standard resist

    500rpm 6s

    750rpm 6s

    3500rpm 30s

    total resist thickness: 1.5-2 μm

36. Prebake 30min

37. Pattern resist using mask 2 (small well)

    ks2aligner (time?)

38. Develop >90s (OOCG 934 3:2)

39. STS etch silicon (small well)

    60μm etch

    Recipe: MIT47

40. Piranha clean
41. STS etch silicon (large well)
    20μm etch
    Recipe: MIT47
42. Strip oxide
    BOE
    5min

Back:

[TRL]

43. HMDS
44. Resist coat
    thick resist(AZ4620) 10μm
    1750rpm 9S
    4000rpm 60s
    7000rpm 10s
45. Prebake
46. Expose using mask 3 (large well)
    Ksaligner2
    IR alignment
    350s
47. Develop 4min (AZ440)
48. Attach wafer to quartz handle wafer
    Use photoresist and jig
49. Postbake
50. STS etch large well through wafer with timed etch to intersect 20μm into small channel
    Timed etch
    Recipe: MIT59
51. Separate wafer from handle wafer in acetone

8 BIBLIOGRAPHY

1. Voldman, J.V., *et al., adapted from NSF SGER Grant Proposal submitted by our group (Voldman, Braff, Schmidt, Gray, Toner).* 1998.
2. Kovacs, G.T.A., K. Petersen, and M. Albin, *Silicon Micromachining Sensors to Systems.* Analytical Chemistry, 1996. **68**(13): p. 407A-412A.
3. Wise, K.D. and K. Najafi, *Microfabrication Techniques for Integrated Sensors and Systems.* Science, 1991. **254**: p. 1335-1342.
4. Fluitman, J., *Microsystems Technology: Objectives.* Sensors and Actuators A, 1996. **56**: p. 151-166.
5. Liu, C.-C. and Z. Jin, *Applications of Microfabrication and Micromachining Techniques to Biotechnology.* Trends in Biotechnology, 1997. **15**: p. 213-216.
6. Sato, K., *et al., Individual and Mass Operation of Biological Cells using Micromechanical Silicon Devices.* Sensors and Actuators, 1990. **A21-A23**: p. 948-953.
7. Bousse, L., *et al. Silicon Micromachining in the Fabrication of biosensors Using Living Cells.* in *IEEE Solid-State Sensor and Actuator Workshop.* 1990. Hilton head, SC.
8. Bousse, L., *et al., Micromachined Multichannel Systems for the Measrement of Cellular Metabolism.* Sensors and Actuators B, 1994. **20**: p. 145-150.
9. Bousse, L. and W. Parce, *Applying Silicon Micromachining to Cellular Metabolism.* IEEE Engineering in Medicine and Biology, 1994. **13**(3): p. 396-401.
10. Bousse, L., *Whole Cell Biosensors.* Sensors and Actuators B, 1996. **34**: p. 270-275.
11. Price, J.A.R., J.P.H. Burt, and R. Pethig, *Applications of a New Optical Technique for Measuring the Dielectrophoretic Behavior of Microorganisms.* Biochimica et Biophysica Acta, 1988. **964**: p. 221-230.
12. Fuhr, G., *et al., Dielectrophoretic Field Cages: Technique for Cell, Virus and Macromolecule Handling.* Cell. Eng. inc. Molecular Eng., 1995. **1**: p. 47-57.
13. Fuhr, G. and S. Shirley, *Biological Applications of Microstructures*, in *Topics in Current Chemistry.* 1998, Springer Verlag: Berlin Heidelberg. p. 83-116.
14. Pethig, R. *Application of A.C. Electrical Fields to the Manipulation and Characterisation of Cells.* in *Automation in Biotechnology.* 1990: Elsevier Science Publishers.
15. Pethig, R., *Dielectrohoresis: Using Inhomogeneous AC Electrical Fields to Separate and Manipulate Cells.* Critical Reviews in Biotechnology, 1996. **16**(4): p. 331-348.
16. Schnelle, T., *et al., Three Dimensional Electric Field Traps for Manipulation of Cells- Calculation and Experimental Verification.* Biochimica et Biophyica Acta, 1993. **1157**: p. 127-140.
17. Beatty, C.C. *A Chronology of Thermal Ink-Jet Strucures.* in *Solid-State Sensor and Actuator Workshop.* 1996. Hilton Head, S.C.
18. Chen, J. and K.D. Wise. *A High-Resolution Silicon Monolithic Nozzle Array For Inkjet Printing.* in *Transducers '95.* 1995. Stockholm, Sweden.

19. Westberg, D. and G.I. Andersson. *A Novel CMOS-Compatible Inkjet Head.* in *Transducers '97.* 1997. Chicago.
20. Lin, L., A. Pisano, and A. Lee. *Microbubble Powered Actuator.* in *Transducers '91.* 1991.
21. Lin, L. and A. Pisano, *Bubble Forming on a Micro Line Heater,* in *ASME Microechanical Sensors, Actuators, and Systems,* D. Cho, *et al.*, Editors. 1991. p. 147-163.
22. Evans, J., D. Liepmann, and A.P. Pisano. *Planar Laminar Mixer.* in *MEMS '97.* 1997.
23. Tong, L.S. and Y.S. Tang, *Boiling Heat Transfer and Two-Phase Flow.* second edition ed. 1997, Washington, D.C.: Taylor and Francis.
24. Cole, R. and S. Van Stralen, *Boiling Phenomena.* Vol. 1. 1979: Hemisphere Publishing Corporation.
25. Firebaugh, S.L., K.F. Jensen, and M.A. Schmidt, *Investigation of High-Temperature Degradation of Platinum Thn Films with an In Situ Resistance Measurement Apparatus.* Journal of Microelectromechanical Systems, 1998. **7**(1): p. 128-135.
26. Mullins, W.W., *Theory of Thermal Grooving.* Journal of Applied Physics, 1957. **28**(3): p. 333-339.
27. Srolovitz, D.J. and M.G. Goldiner, *The Thermodynamics and Kinetics of Film Agglomeration.* Journal of Metals, 1995: p. 31-36.
28. Lin, L., *Selective Encapsulations of MEMS: Micro channels, needles, resonators, and electromechanical filters,* in *Mechanical Engineering.* 1993, University of California, Berkeley: Berkeley, CA.
29. Carslaw, H.S. and J.C. Jaeger, *Conduction of Heat in Solids.* 1959, London: Oxford University Press.
30. Takematsu, M., *Slow viscous Flow Past a Cavity.* Journal of the Physical Society of Japan, 1966. **21**(9): p. 1816-1821.
31. Taneda, S., *Visualization of Separating Stokes Flow.* Journal of the Physical Society of Japan, 1979. **46**(6): p. 1935-1942.
32. Shen, C. and J.M. Floryan, *Low Reynolds Number Flow over Cavities.* Physics of Fluids, 1985. **26**(11): p. 3191-3202.
33. Davis, R.H., *Velocities of Sedimenting Particles in Suspensions,* in *Sedimentation of Small Particles in a Viscous Fluid,* E.M. Tory, Editor. 1996, Computational Mechanic Publications.
34. Happel, J. and H. Brenner, *Low Reynolds Number Hydrodynamics.* 1965, Englewood Cliffs, N.J.: Prentice-Hall, Inc.
35. Srinivasan, R., *Microfabricated Reactors for Partial Oxidation Reactions,* in *Chemical Engineering.* 1998, Massachusetts Institute of Technology: Cambridge, MA.
36. Touloukian, Y.S., ed. *ThermophysicalProperties of High Temperature Solid Materials.* . Vol. 1. 1967, The Macmillan Company: New York.